Studies on Aero-Thermal Performances of Leakage Flows Injection from the Endwall Slot in Linear Cascade of High-Pressure Turbine

Wan Aizon W Ghopa

A dissertation submitted in partial fulfillment
of the requirements for the degree of

Doctoral of Philosophy

Mechanical System Engineering
Iwate University
2013

Dissertation Committee;

Professor Ken-ichi FUNAZAKI
Professor Hideki YANAOKA
Professor Kazuyuki UENO

Abstract

Present studies focus on thermal and aerodynamics investigations of leakage flow injection through a slot which is located at upstream of blade leading edge. In the real gas turbine, this slot is actually the gap between the combustor and turbine endwall as for the maintenance works consideration. However, the slot induced to the leakage phenomenon caused by the bypassed air that coming from the compressor side for turbine cooling purposes. Gas turbine manufactures intended to minimize these kinds of leakages in maintaining the aerodynamics performance of the turbine cascade. However, previous researchers found that the leakages could be used to protect the endwall surfaces from the hot gas since it could not be completely prevented. Thus, present study investigated the potential of leakage flows as a function of film cooling. Chapter 1 gives some introduction on present works about the need of film cooling to protect the wall surfaces. Several related studies by previous researchers are also explained. Chapter 2 explained the details of methodologies used in present studies. A leakage flow with 90° of injection angle was considered as for the baseline configuration. Liquid crystal was used for the time-varying endwall temperature measurement. The transient method was applied to determine the film cooling effectiveness, η and the heat transfer coefficient, h for the thermal performance evaluations. The details of the aerodynamics performances was revealed by conducting 5-holes Pitot tube measurement at blade downstream plane ($1.25C_{ax}$) and the total pressure loss coefficient, C_{pt} as well as the flow vorticity, ζ contours were plotted. Furthermore, the effects of the leakage flow with the mainstream consist of complex secondary flows structures also have been revealed by numerical investigation. In present study, the flow is analyzed by using the three-dimensional, steady Reynolds-averaged Navier-Stokes (RANS) equations by conducting Shear Stress Transport, SST turbulence model. The leakage was injected with a various amount (which is described by mass flow ratio, MFR) to observe the η performance at different injection cases. Chapter 3 provided details discussions on the aero and thermal performances of the leakage injection. Both experimental and numerical presented the performance of η increased when the injection amount increases. SST turbulence model captured the presence of the separation flow that caused the lower h region which also captured by the experimental. As for the aerodynamics performance, C_{pt} was increased after the introduction of leakage injection and indicated the increase trend when the MFR was being increased. Leakage flows were

prevented to be injected into high pressure region thus they tended to move towards lower pressure region which is between two stagnation regions. As a result, a newly generated vortex core was predicted. This accumulated vortex core (AFV) is considered to contribute to the additional losses at blade downstream. Chapter 4 presents the numerical investigation on the modification of slot configurations such as positions and orientations. The leakages flow by shallower injection angle, β towards mainstream was predicted to reduce the strength of the passage vortex thus increase the aerodynamics performance particularly at higher injection cases. Additionally, η also obviously increased by the slot orientation. To move away the slot from the blade LE was predicted to increase both aero and thermal performance. The leakage flow could laterally be penetrated to the mainstream and stayed closer on endwall surfaces. This is due to the fewer blockages influenced by the stagnation region since the slot located far away from the blade LE. In contrast, move the slot closer towards blade LE just increased the $C_{pt.}$ Furthermore, locate the slot closer to blade LE could not increase the protection layer except the level of η. Finally, Chapter 5 highlights the important points to be concluded based on present investigations. The potential of the leakage flows to protect the endwall surfaces has been proven and they were highly influenced by the secondary flows behavior on the endwall region. However, to increase the performance of cooling by increasing the injection amounts unfortunately reduces the aerodynamics performance due to the increase strength of the secondary flow vortices. The leakage flow with a shallow injection angle towards mainstream are predicted to provide a positive trends of cooling performance with a lower aerodynamic losses especially at higher leakage flow injection cases.

Keywords: Turbomachinery, secondary flow, endwall film cooling, leakage flow, purge flow, heat transfer, high-pressure turbine, liquid crystal, transient method, pressure loss, slot orientation, slot position.

ACKNOWLEDGMENTS

Firstly, I would like to express my sincere appreciation to my advisor, Professor Ken-ichi Funazaki, for his valuable advices and guidance that he offered me throughout these years. His generous support and constant encouragement in my research activities made me never give up and always keeps me on moving forward.

Highly grateful to the Dissertation Committee, Professor Yasaoka and Professor Ueno who have kindly provided their suggestions and comments to improve the dissertation. Also appreciating to them for their time in evaluating this dissertation.

Thanks are also to the staff of the workshop center in Iwate University especially Mr. Mamoru Kikuchi who always produced work of unrivalled caliber. I am also grateful to Associate Professor Taniguchi and Dr. Kato for their many supports, discussions and ideas in experimental and numerical simulation works. Colleagues of the Aero-engine Laboratory have not only provided me a kind environment but also a valuable source of assistance and friendship. Many thanks also to Mr. Kawabata and former doctoral course candidate, Dr. Kamil Abdullah for their kind help and supports.

I am deeply indebted to my research partner, Mr. Miura Takemitsu, whose currently working at Hitachi and Mr. Ito Ken-ichi currently working in Tokyo and Mr. Suzuki Yuuya who will continues the research activities. I believed that they did their best in helping me especially in experimental works.

Thank you to Hitachi Ltd for their financial support in developing a new wind tunnel and etc. Great thanks also to my employer, National University of Malaysia (UKM) and Ministry of High Education, Malaysia (MOHE) for their funding during my study period.

Of course cannot be denied a very special acknowledgment must be given to my parent and siblings who always give me a moral support and continuously pray for my success.

Last but not the least very special mention to my family especially my lovely wife who always stands right beside me since I was in secondary school is actually one of the key of my success.

Table of Contents

List of Figures

List of Tables

NOMENCLATURE

Latin letters

A	Sectional area
c	Specific heat
C	Actual blade chord
C_{ax}	Axial blade chord
CR	Convergence ratio
C_{ps}	Static pressure loss coefficient
C_{pt}	Total pressure loss coefficient
$\overline{C_{pt}}$	Area-averaged total pressure loss coefficient
C_{SKE}	Secondary kinetic energy coefficient
D_{acc}	Accuracy of the device
h	Heat transfer coefficient
l	Distance of slot from blade leading edge
$\dot{m}$	Mass flow rate
MFR	Mass flow ratio
n	number of pitch
P_d	Dynamic pressure
P_s	Static pressure
P_t	Total pressure
Q	Volume flow rate
Re	Reynolds Number
SKE	Secondary kinetic energy
T	Temperature
t	Time
U	Absolute velocity
u	Axial velocity component
v	Pitch wise velocity component
V_{ax}	Axial flow velocity direction
w	Span wise velocity component

x/C_{ax}	Normalized-axial direction
y/p	Normalized-pitchwise direction
z/s	Normalized-spanwise direction

Greek letters

α	yaw angle
β	leakage flow injection angle
ρ	Density
ζ	Vorticity
δ	Boundary layer thickness
δ_D	Device accuracy uncertainty
σ	pitch angle
ε	Standard deviation
η	Film cooling effectiveness
$\bar{\eta}$	Area-averaged film cooling effectiveness

Subscripts

ave	Average
aw	Adiabatic wall
Max	Maximum
Min	Minimum
mid	Mid span
out	Outlet
∞	Mainstream at inlet
2	Secondary

Acronyms

CFD	Computational fluid dynamic
EFD	Experimental fluid dynamic
HSL	Hue, saturation and light
LE	Leading edge
PS	Pressure side
SS	Suction side
SST	Shear Stress Transport
RGB	Red, green and blue
TE	Trailing edge
TLC	*Thermo-cromic* liquid crystal

Chapter 1

Introduction

This chapter provides some introduction on the gas turbine technologies. Increasing gas turbine thermal efficiency is an approach to increase the performance which leads to increase of turbine inlet temperature. The need of film cooling to protect the material surfaces from the hot gases is also explained to show it's a very effective way to allow further increases of turbine inlet temperature. In addition, the literature study has been done to investigate the current achievement of the gas turbine cooling focusing on the endwall side. The research objective is also includes in this chapter.

Background

Gas turbines are used to power aircrafts, trains, ships and electrical generators. Figure 1 illustrates the gas turbine structure of HF120 Turbofan manufactured by General Electric and Honda whereas Figure 2 shows the diagram of modern gas turbine. Generally, gas turbine can be divided into three sections; compression, combustion and expansion. The air flows through a fan which then be compressed with multistage compressor to a higher pressure. Energy is then added by injecting fuel into the compressed air inside the combustion chamber and igniting it so a high temperatures flow is generated in this stage. This high-temperature and high pressure gas enters a turbine, where it expands down to the exhaust pressure, producing a shaft work or thrust output in the process. The turbine shaft work is used to drive the compressor and other devices such as an electric generator that coupled to the shaft. The energy that is not used for shaft work comes out in the exhaust gases, so these have either a high temperature or a high velocity. The HF120 Turbofan is a gas turbine used for the jet

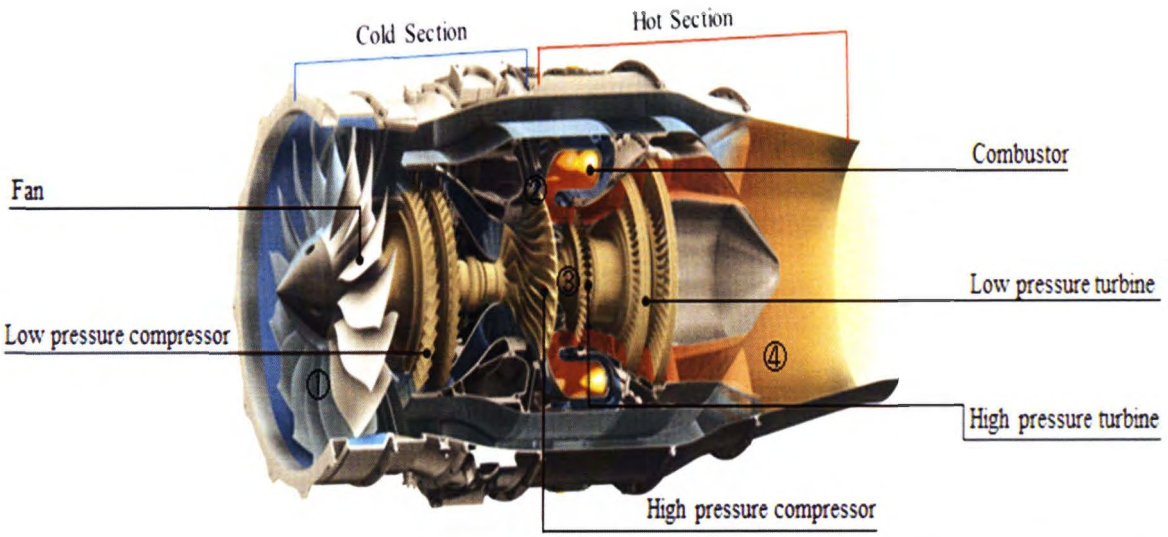

(Source: Adapted from GE Honda link [35])

Figure 1 Gas turbine structure- HF120 by GE Honda

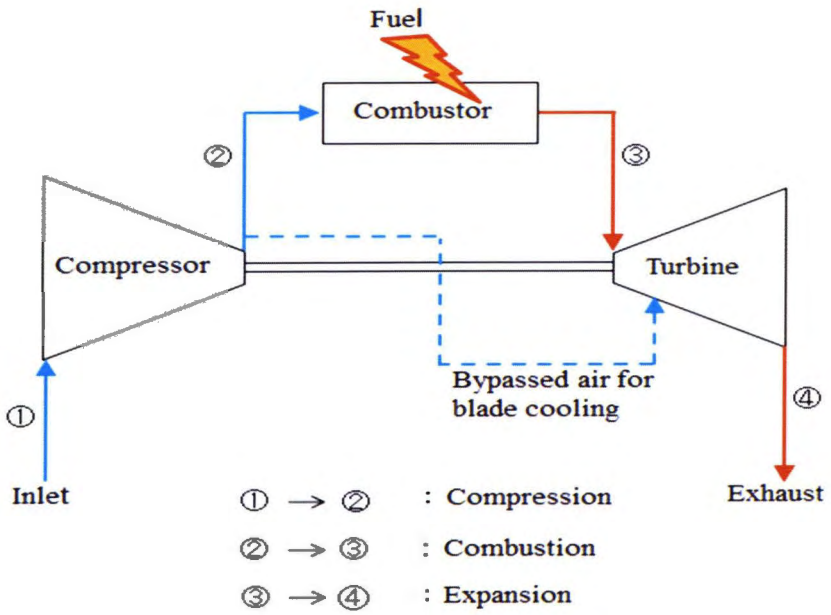

Figure 2 Diagram of modern gas turbine with cooling technology

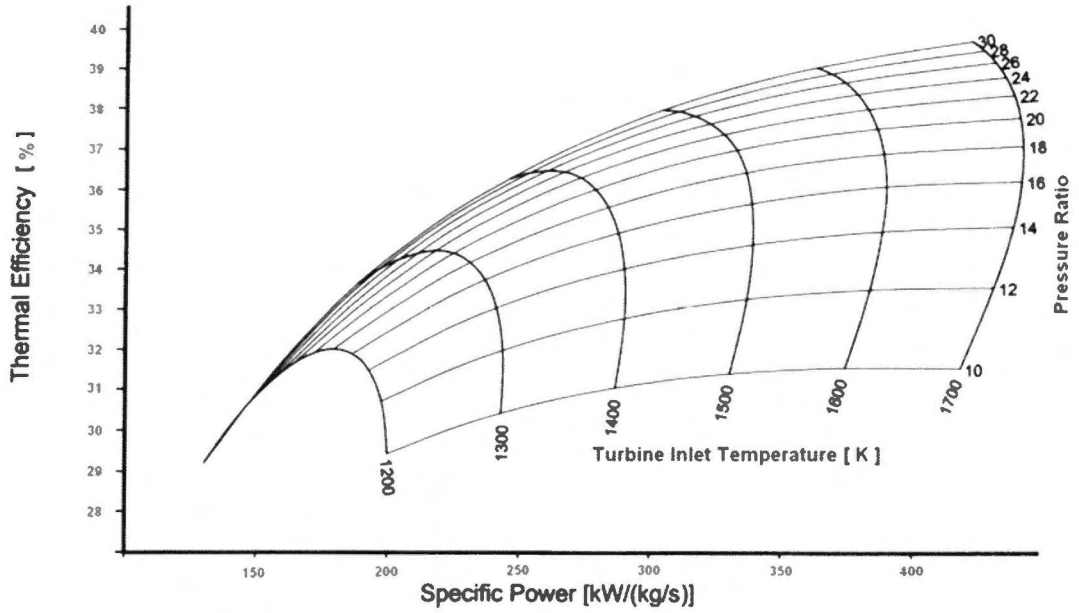

(Source: Genrup, 2005 [36])

Figure 3 Modern gas turbine performance chart

engines which are optimized to produce thrust from the exhaust gases, or from ducted fans connected to the gas turbines.

Now day's modern gas turbines have to fulfill the requirements of an increasing efficiency combined with very low emissions in a robust, cost-effective way. Indeed, a global warming due to the greenhouse effect is one of the most issue has been discussed and need to be prevented. Low emissions or reducing the fuel burning is considerable limited the amount of carbon dioxide gas released into the atmosphere. This can be realized by increasing the gas turbine thermal efficiency. Looking at the performance chart for the design of a modern gas turbine, see Figure 3, it is obviously that the need to achieve higher total gas turbine efficiency leads to an increase of the turbine inlet temperature. To take advantage of the higher turbine inlet temperature the turbine pressure ratio also has to be increased. The trend of increasing turbine inlet temperatures started in the 1940`s with the first jet engines proposed by Sir Frank Whittle and continues to modern gas turbines as shown in Figure 4. As it can be recognized from Figure 4, the increase in turbine inlet temperature has proceeded much faster than the progress in the development of more advanced vane and blade materials. Indeed turbine inlet temperature levels exceeded maximum tolerable material temperature by several hundred K starting in the 1960`s, and this trend has continued since ever. This

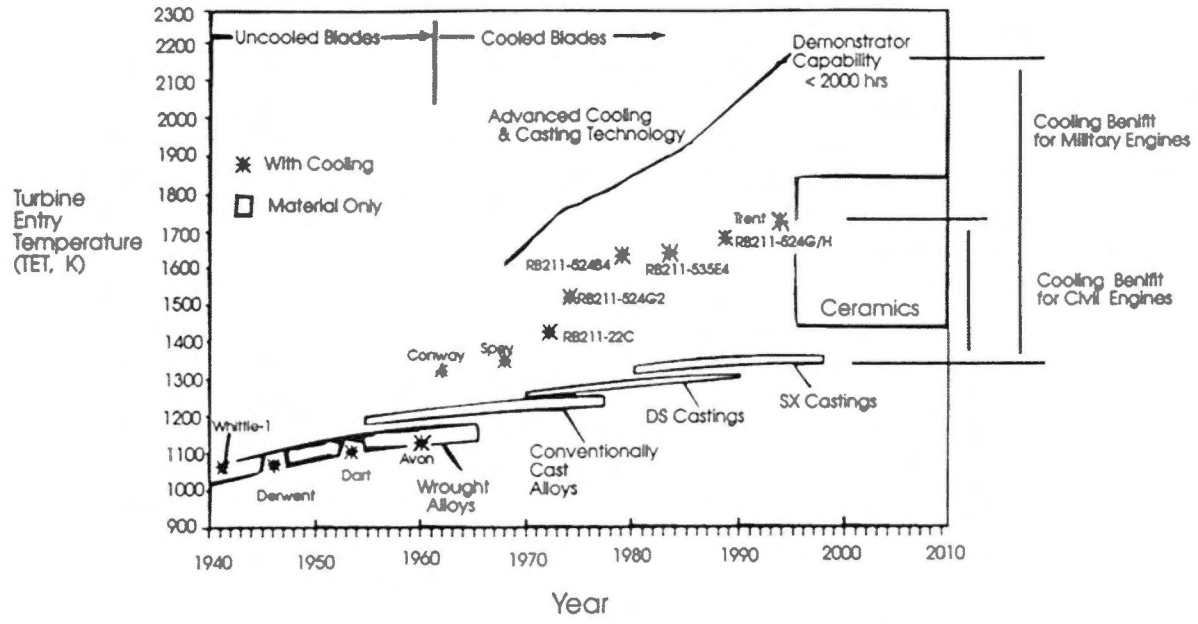

(Source: Royal Aeronautical Society/Aerospace, 1994)

Figure 4 Turbine inlet temperature based on advanced material and cooling technology

condition is realizable only through the application of advanced vane and blade cooling technology to keep the material temperature below the allowable, lifetime-limiting level. The extraction of the compressed cooling air bypassing the combustion chamber (as shown in Figure 2) leads to an additional increase of the already high turbine inlet temperature. These effects lead to a very high heat load of the nozzle guide vane hub and tip endwall of a modern gas turbine. This implicates that the endwall have to be provided with an advanced cooling technology to achieve the required lifetime-limiting material temperature.

Film cooling is an effective way to protect blade or endwall surfaces from the extremely high temperature gases. Figure 5 shows on how the ejected coolant into the mainstream produces the protection layer close to the endwall surfaces that mostly called film cooling. The coolant temperature, T_2 with a blue streamline is injected through holes or slot on endwall into the high temperature of the main flow, T_∞ indicated by the red streamline. Downstream of the hole or slot exit, the coolant will stay closer to the endwall surfaces and providing a layer which preventing the endwall surface not to be directly expose to the hot gas. Thus, the gas turbine can be operated at higher temperature exceeding its thermal stress limit since the material surfaces are protected by the film cooling. Film cooling effectiveness

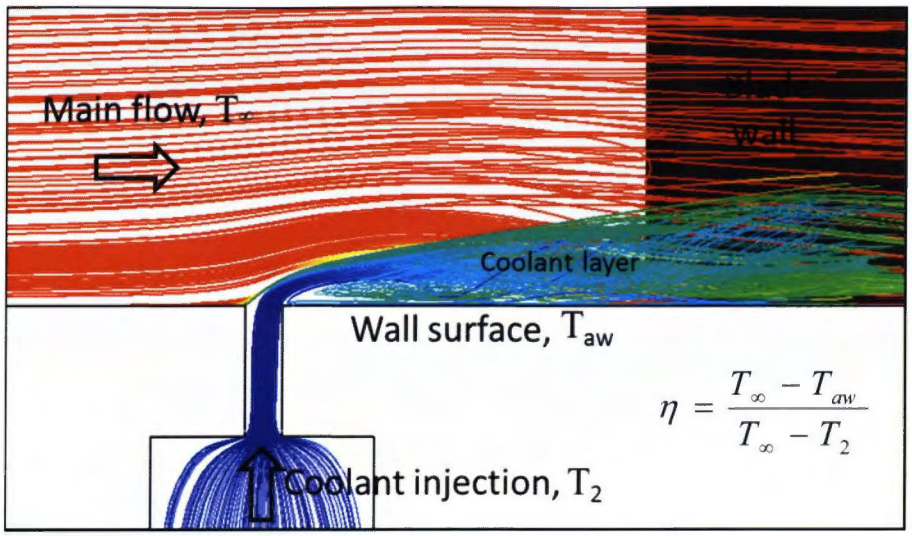

Figure 5 Film cooling concept

is a normalized temperature usually represented by η is a parameter used to evaluate the performance of film cooling. The high pressure turbine is just located downstream of the combustor chamber, thus the film cooling approaches are required at this stage. Figure 6 shows an example of the modern cooled gas turbine blade with film and internal blade cooling. As been discussed, the film cooling has not only been employed on the blade surface but also on the endwall of the turbine blade to provide necessary cooling protection for the component. As shown in the diagram from Figure 2, the extraction of the air from the high pressure compressor side unfortunately leads to the leakage phenomenon through the slots exist in high pressure turbine stage. Figure 7 shows the real high pressure turbine blade with cooling holes design on blade and endwall surfaces. According to the Figure 7, there are two locations of slots exist in high-pressure turbine stage. First slot is actually the gap between the combustor and turbine endwall located at upstream of blade leading edge while the second slot is the gap between the blade segments, respectively. The blade was split into several segments as for the maintenance works consideration. Gas turbine manufactures intended to minimize these kinds of leakages in maintaining the aerodynamics performance of the cascade. However, previous researchers found that the leakages through the upstream slot could be used as cooling air to protect the endwall surfaces from the hot gas since it could not be completely prevented. In addition, the high pressure from the leakage air also prevents the hot mainstream air ingestion into these gaps. For the cooling purpose, endwall side is

considered more difficult than the blade surfaces due to the presence of the complex secondary flows structures which was believed to give a high impact on the heat transfer performance. Thus, the understanding of the endwall flow structures is highly important in this study in order to see their interaction with the coolant flow. The details of the secondary flows in the cascade are firstly explained in the next section.

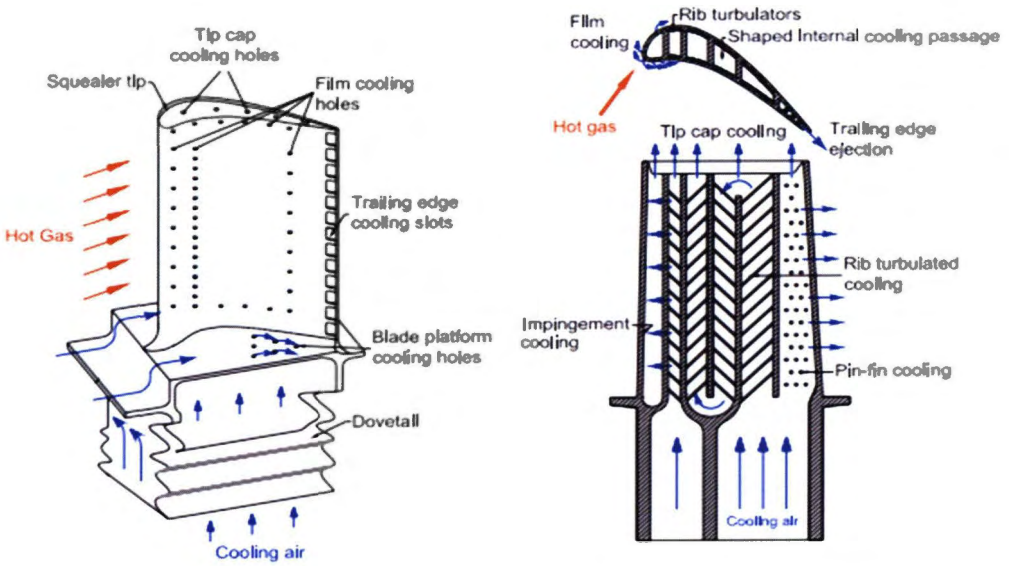

(Source: Adapted from Han et al. [37])

Figure 6 Modern cooled gas turbine blade

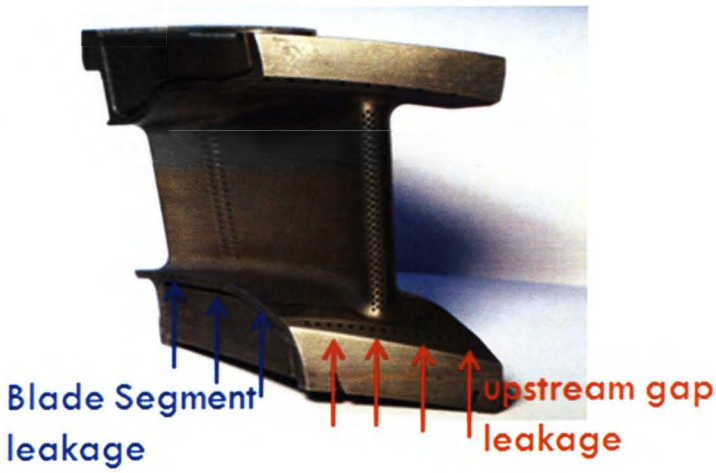

(Source: Adapted from Frank G. R., 2006 [38])

Figure 7 Leakage phenomenon influenced by bypassed cooling air in HPT

1.1 Secondary flows in the blade passage

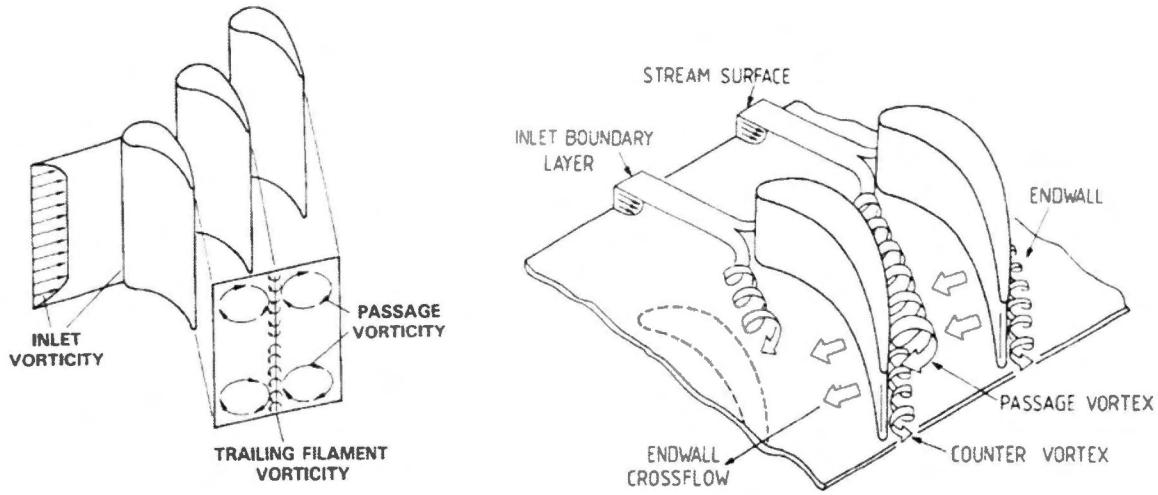

(a) (b)

Figure 8 Secondary flow system; (a) Hawthorne, 1955, (b) Langston, 1977

Secondary flow structure generated in the blade row is the main factor that contributes to the endwall loss. Since the secondary flow is a result of viscous shear on the endwall, it is a large source of loss, contributing approximately one third of the total loss, Denton [1]. A common means of quantifying secondary flow is by its Secondary Kinetic Energy (SKE), which is normally defined as the kinetic energy associated with the velocity components perpendicular to the primary flow direction. In the classical secondary flow system, Hawthorne [2], the axis of vorticity is twisted as the flow passes through the blade passage. This axis is initially perpendicular to the flow direction, as it is caused by viscous effects in the boundary layer, but by the blade row exit two counter-rotating passage vortices have been formed, see Figure 8 (a). The vortex sheet also contains trailing filament vortices, which are caused by the radial change in blade circulation, Sieverding [3]. The inlet end wall boundary layer rolls up in front of the leading edge to form the horseshoe vortex, as first seen by Klein [4]. Measurements by Langston et al. [5], showed the evolution of the vortex through the blade row, Figure 8 (b): the pressure surface leg moving across the passage, due to the cross-passage pressure gradient, and merging with the passage vortex. The horseshoe vortex increases the SKE of the passage vortex by approximately 20 %, Georgiou et al. [6]. Sharma and Butler, [7], showed that the suction surface leg of the horseshoe vortex lifts up the blade

surface where the separation line reaches the blade surface. It then orbits around, and is dissipated by, the passage vortex, although this type of interaction is dependent upon the particular cascade geometry and pressure ratio, Goldstein and Spores [8]. Any reduction or elimination of the leading edge horseshoe vortex is thought to have little effect on the shape and position of the passage vortex, Sieverding [3]. In addition to the horseshoe and passage vortices, several other vortices were found by Goldstein and Spores [8], see Figure 9. Sharma and Butler [9] also present a complex secondary flow models, shown in Figure 10. Wang et al. [10] also presented the flow field data within the vane stagnation plane illustrating the formation and dynamics of the leading edge horse-shoe vortex. The strongest is the corner vortex found in the suction surface end wall corner, which rotates in the opposite sense to the passage vortex. It is formed in a similar manner to the horseshoe vortex where the limiting streamline impinges on the suction surface near the position of maximum surface curvature, Sieverding [3], but is only formed when the blade loading is sufficiently high to give a strong interaction of the passage vortex with the blade surface. Its existence is shown by the radial angle distribution, which gives a reduction in overturning near the end wall, Gregory-Smith and Graves [11].

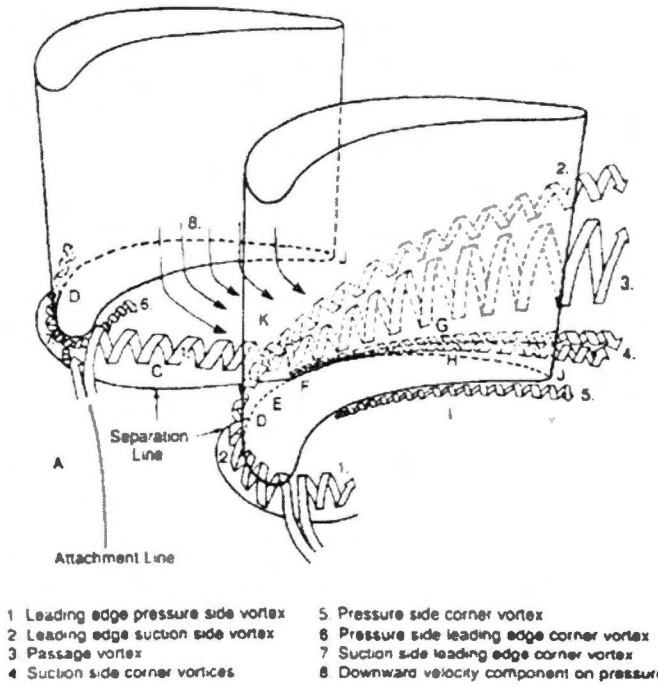

Figure 9 Endwall flow field, Goldstein and Spores, 1988

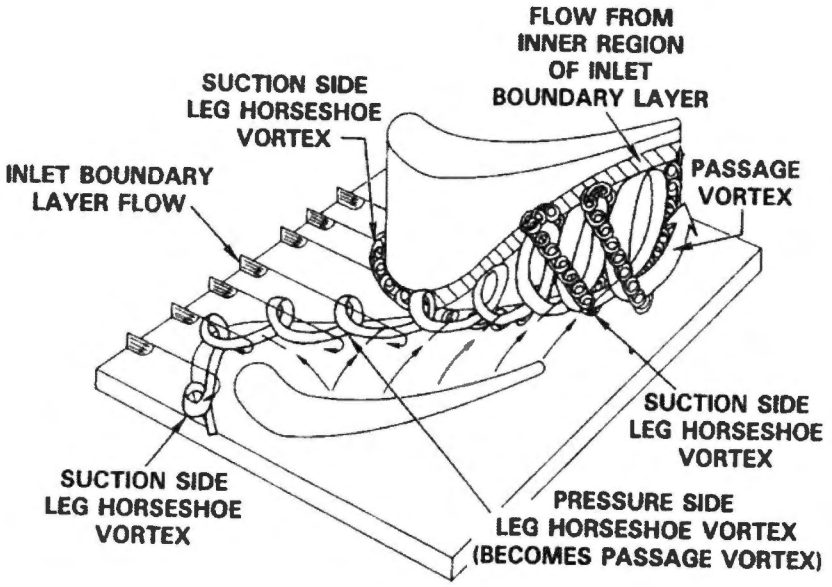

Figure 10 Cascade endwall flow structure by Sharma and Butler, 1996

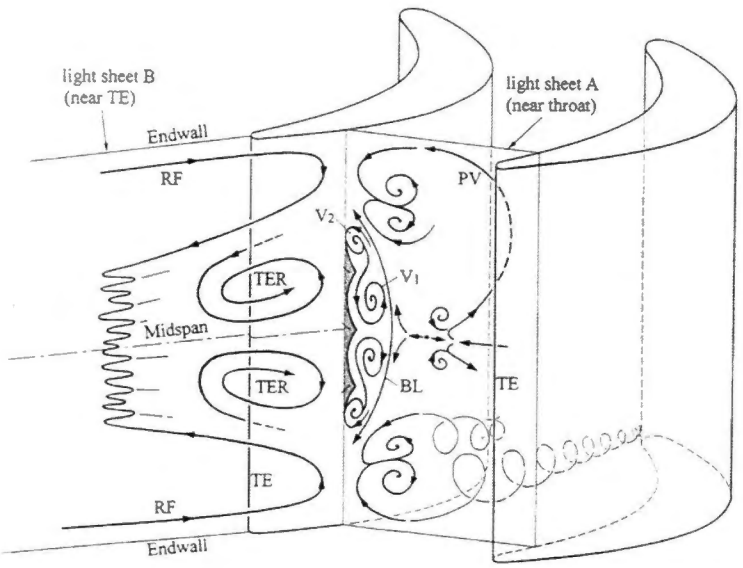

Figure 11 Detailed vortex system, Yamamoto et al., 1995

An investigation of the flow field downstream of the corner formed by a blade and a flat plate showed that the corner vortex dissipated quickly, disappearing by approximately 20 % chord length downstream, Abdulla-Altaii and Raj [12]. A pair of three-dimensional vortices, V_1 and

V_2, was also found inside the suction surface boundary layer, *BL*, near the trailing edge, *TE*, Yamamoto et al. [13], Figure 11: some of this low energy fluid is absorbed into the passage vortex, *PV*. Near the suction surface trailing edge, there are strong reverse flows towards the throat, *RF* and *TER*, and some of the vortices behave unsteadily due to the surrounding vortex movement. Having described the secondary flow structure, the corresponding losses can also be examined. There are three characteristic loss features at the trailing edge plane as well as the end wall boundary layer. Dependent upon the inlet boundary layer thickness and blade loading, these are more or less superimposed and as the loading increases they lift off from the end wall. The secondary flow strength is largely dependent upon the thickness of the upstream boundary layer and the amount of turning in the blade row, Sieverding [3]. Since dissipation within a vortex core is very high, the decay of the SKE yields an increase in entropy, Denton, [1]. Although some of the dissipation occurs within the blade row, most occurs after the trailing edge and it is often assumed that all the SKE is lost: although this exaggerates the loss, it partially accounts for other losses, such as the mixing losses, Sieverding [3]. The sum of the loss coefficient and the SKE was found to be approximately constant at any plane downstream of a two dimensional blade trailing edge, as was the mixed out loss, Moore and Adhye [14], implying that the decay in SKE closely matches the increase in entropy.

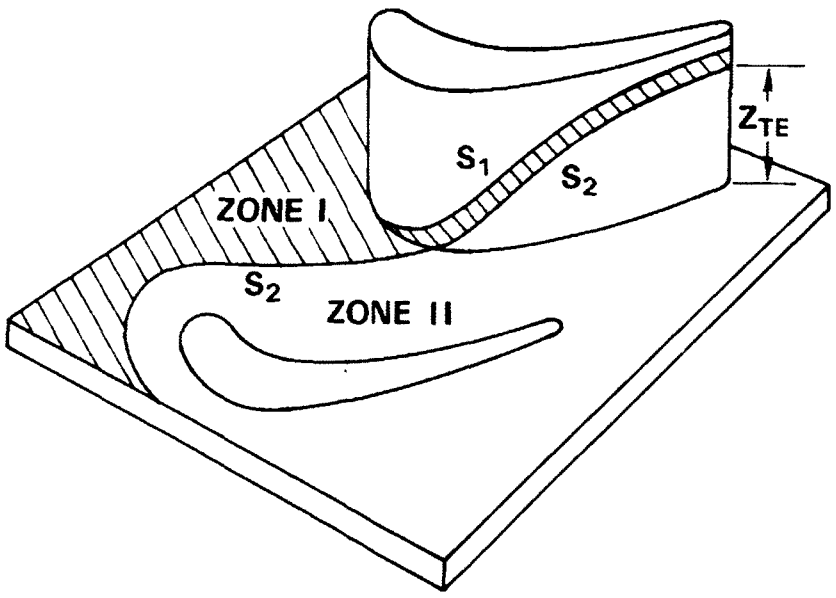

Figure 12 Endwall separation lines, Sharma and Butler, 1986

A method to estimate the endwall losses was developed by Gregory-Smith [15], showing a good agreement with experimental data: however, this was dependent upon the detailed blade design. It was later suggested that an indication of the strength of the endwall loss was the height of the separation line on the suction surface trailing edge, Sharma and Butler [7], see Figure 12, termed the penetration height, Z_{TE}. This correlation is only dependent upon the flow turning angle, α, the convergence ratio of the blade row, CR, and the ratio of the inlet boundary layer height, to the blade height, δ_1/h:

$$\frac{Z_{TE}}{C} = 0.15\frac{\alpha}{\sqrt{CR}} + 1.4\frac{\delta_1}{h} - 2.73\left(\frac{\delta_1}{h}\right)^2 + 1.77\left(\frac{\delta_1}{h}\right)^3 \quad (1)$$

1.2 Relevant studies by previous researchers

Previous section discusses on the existence of the secondary flows on the endwall region of the cascade without any disturbance from coolant air injection or by the effect of different inlet flow parameters. The study above clearly explained that the needs of the details investigation not only in the heat transfer behavior but also the interaction between complex secondary flows with the coolant air. These all information is required for the development of the modern gas turbine. This section will discuss about the related studies made by other researches for the endwall film cooling especially through the slot leakage air approach. Some other researcher defined as 'purge flow' if it is intended to inject the air from the slot for the cooling purpose. Studies by Kang et al. [16] and Radomsky and Thole [17] revealed the effect of inlet Reynolds number and turbulence level respectively on the formation of the horse-shoe vortex. Both studies were not included the purge flows. Using the same cascade of the previous study [16, 17], Sundaram and Thole [18] performed LDV measurements to reveals the effect of the purge flow on the endwall flow structure to enable direct comparison with the previous result [16, 17]. Rehder and Dannhauer [19], has carried out the experiments to reveal the effects of injection flow angle from the upstream clearance of linear cascade of LPT stator vanes. The observation shows that the leakage ejection perpendicular to the main flow direction amplifies the secondary flow, in particular the horse-shoe vortex and therefore

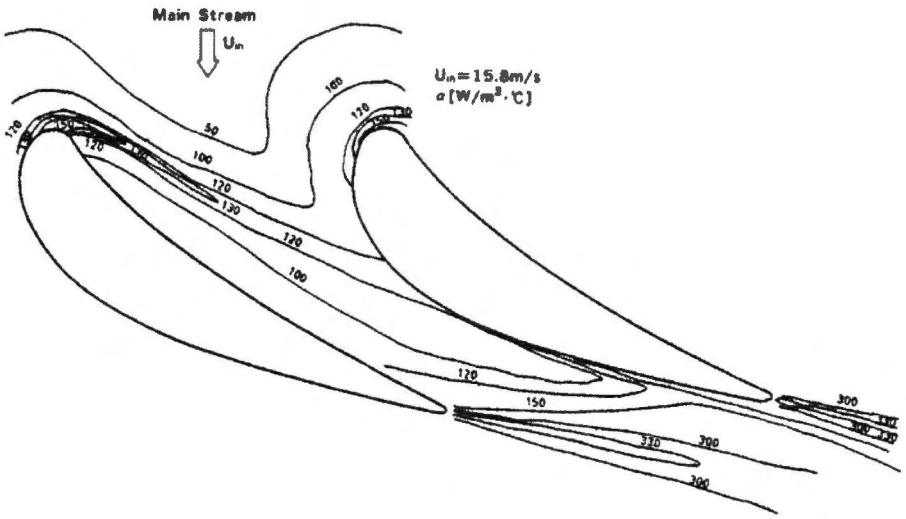

Figure 13 Endwall heat transfer distribution in cascade by Takeshi et al, 1990

increases the secondary losses near the endwall region, whereas tangential leakage ejection causes significant reduction of horse-shoe vortex and at the same time decreasing the secondary losses at the cascade exit. Recently, Thrift and Thole [20] investigated the effects of orientation and position of the purge flow. The observations show a dramatic difference in horse-shoe vortex formation at the stagnation plane which is directly influenced by the orientation and position of the purge flow. The earliest study that relates the endwall flow structure and film cooling has been made by Blair [21]. The work clarifies that, the horse-shoe vortex and passage vortex has a dominant impact on the heat transfer of film-cooled endwall. This also was proved by Takeshi et al. [22], as shown in Figure 13. They found that the heat transfer distribution on a vane passage endwall with the increased heat transfer in the leading edge region caused by the horse-shoe vortex. The heat transfer increased along the separation line and in the airfoil wake region. They also found a reduction of the endwall film cooling effectiveness near the blade leading edge due to the presence of the horse-shoe vortex. Blair [23] reported a slight increase of the heat transfer in the beginning of the flow passage with increasing Reynolds number due to earlier transition of the boundary layer. Further downstream, the heat transfer decreases at higher Reynolds numbers because of the thicker turbulent boundary layer. Again, higher heat transfer in the trailing edge wake region at the lower Reynolds number can be observed. Kost and Nicklas [24] presented aerodynamic measurement from a transonic cascade with an upstream normal leakage ejection located at $0.2C_{ax}$. They found that injection at this location promoted the separation and enhanced the

horse-shoe vortex. Kost and Mullaert [25] continued the study by moved the slot location to $0.3C_{ax}$ upstream of the cascade. From the results obtained, they found that the slot flow stayed closer to the endwall and provided better film cooling than flow from the slot located at $0.2C_{ax}$ of cascade upstream. With 45 degree of leakage slot injection, Lynch and Thole [26] and Knost and Thole [27] performed adiabatic effectiveness experiments by a different slot location which was located at $0.96C_{ax}$ and $0.38C_{ax}$ upstream of the vane cascade respectively. It was noted that the coverage area of the leakage coolant was similar between the two locations. The effectiveness levels within the passage, however, were lower for the slot placed further upstream as the coolant had more distance to mix with the hot mainstream flow. The upstream leakage studies were also done by other researchers such as Piggush and Simon [28], measured heat transfer characteristic over the contoured endwall in the cascade of high-pressure turbine stators by the use of thermocouples on the endwall, emulating the leakage flows from the upstream clearance and the segment gap. The similar study also done by Lynch and Thole [26] using IR camera to determine the heat transfer and film cooling effectiveness distribution over the endwall with the emphasis on gap size. They observed that a narrower gap achieved a relatively uniform leakage flow along the circumferential direction, resulting in a wider coverage of the leakage flow on the endwall. The observations show a dramatic difference in horse-shoe vortex formation near the stagnation region which is directly influenced by the orientation and position of the purge flow. Studies on various test conditions are required to have detailed information on relevant studies. Based on above literatures, it is also clear that cooling air injection from upstream slot highly influenced the aerodynamics performance of turbine cascade. Furthermore, slot location and geometry as well as cooling air amount need to be carefully considered for the optimization purpose. In present works, a new model with slightly lower solidity and higher aspect ratio compared with previous test blade [29] has been designed. The slot location also was moved slightly away from the blade leading edge. The study focuses on both aero and thermodynamics effect of leakage flow on the endwall region of high-pressure turbine linear cascade. Aerodynamic measurements were performed by the use of pneumatic 5-hole pitot tube to measure a total pressure at blade downstream while the liquid crystal was used for the thermal investigation. The numerical simulation was also conducted for the validation and to predict the interaction of ejected leakage flow with the mainstream.

1.3 Research objectives

The objectives of the current study are to reveal the potential of leakage flows in providing the protection layer on the endwall surface in linear cascade of high-pressure turbine. In order to achieve present objectives, the studies concentrate on;

I. Investigation on the interaction between the leakage flow and the mainstream which influenced to the aerodynamics losses and cooling performance
II. Aero-thermal performance based on difference amount of leakage flow ejection
III. The performance of the numerical simulation in predicting the aero-thermal performance by the presence of secondary flow phenomenon on the endwall region
IV. The aero-thermal performance of leakage flow based on modification of slot orientation and position.

Chapter 2

Research Methodologies

This chapter presents the research methodologies implicated in present study. The experiments involve two main experimental procedures (aero and thermal measurement) which are conducted at Iwate University, Japan. Both of the measurements have been conducted in the same experimental setup which enable a directly investigation on the role of aerodynamics behavior onto thermal performance. Numerical simulation is also one of the approaches that were applied in this study in order to reveal the flow which cannot merely investigated by the experimental.

2.1 Test models

The test blade used in present study is shown in Figure 14. The blade design is merit to the first stage turbine which is operating in high pressure condition. The blade was designed by using 3-dimensional CAD (Computational Aided Design) software known as SolidWorks. Based on the 3D data obtained from the SolidWorks, the blade was manufactured by applying a rapid-prototyping method. In order to investigate the effect of the leakage phenomenon in high-pressure turbine cascade, 6 blades have been designed with 5 segments as shown in Figure 15. The two blades with hub endwall are expected to be a measurement region which consisted with a upstream leakage slot along the beginning of the endwall. Two segment leakage gaps also have been design where the first segment gap located between blade 2 and blade 3 while the second segment gap in between blade 4 and blade 5. Upstream slot was designed to have a merit to the gap between the first stage turbine endwall and combustor endwall while the gaps between the blades segments are merit to the

Figure 14 Test blade manufactured by rapid-prototyping method

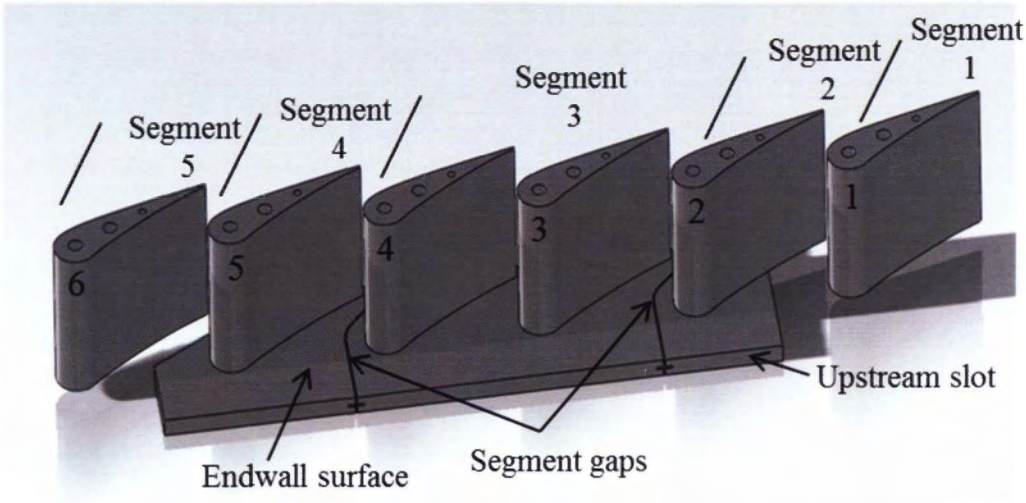

Figure 15 Test blade design-3D CAD image

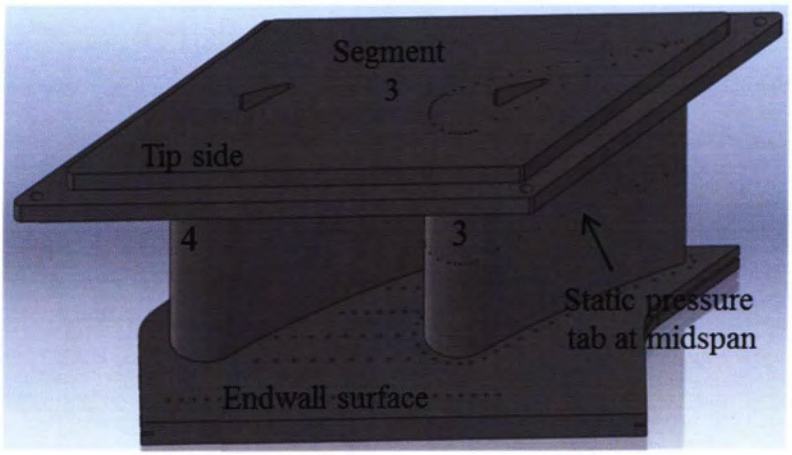

Figure 16 Blade segment 3 with static pressure tabs- 3D CAD image

Table 1 Blade profiles

Parameter	Profile
Span, h	117.68 [mm]
Pitch , t	115.91[mm]
Chord, C	120.23[mm]
Axial Chord, C_{ax}	62.34[mm]
Solidity, C/t	1.02
Aspect ratio, h/C	0.98
Inlet flow angle, β_1	0°
Outlet flow angle, β_2	72.3°
Fillet	No
Upstream gap width	4 [mm]
Segment gap width	1.25 [mm]

gap exist between the blades in the real gas turbine. In actual application, these gaps are designed in consideration of maintenance works where the hub/tip and blades has been split to several parts. However, present study will focuses on the leakage flow from the upstream slot. Figure 16 illustrates the blade model for static pressure measurement where the pressure tab was design on the endwall and mid span of blade PS and SS of blade segment 3. Thus, the test blade can easily be replaced for measurement purpose. The details of the test blade are shown in Table 1.

2.2 Test facility

The new test facility was designed for aerodynamic and endwall temperature measurements of a proposed test model. The experimental investigations were conducted in subsonic wind tunnel located in the Aerospace Laboratory at Iwate University. Figure 17 shows the test apparatus used in this study, indicating main blower, diffuser, settling chamber, contraction nozzle, transition duct and test duct. The main blower was used to drive the mainstream air into the test duct with maximum flow rate of 320 m^3/min at pressure of 3000 Pa. The diffuser is 1500mm long gradually-expanding passage following the test section with inlet size of 390 x 490mm up to 900 x 900mm at exit in which the flow speed decreases and the pressure rises. The flow kinetic energy coming from the main blower was converted to static pressure inside the settling chamber. The uniform flow structures are required to obtain more compatible results with numerical simulation. The modification of the mainstream flow structures was done by applying two screens and honeycomb inside the settling chamber to calm the flow and minimize the disturbances. The settling chamber's cross section dimension is 900 x 900mm and match up with the dimensions of the contraction nozzle. The contraction nozzle's purpose is to take a large volume of low velocity air and reduce it to a small volume of high velocity air without creating turbulence. The length the nozzle is 1100mm. The size of the large end, nearest the settling chamber was set at 900 x 900mm. The small end of the contraction nozzle was set at 580 x 178mm which fixed the size of transition nozzle (300mm length). The flow coming from the transition nozzle will be driven into the test section. The shape of the contraction nozzle was a cubic curve, and the curve was applied on those four surfaces. The secondary blower works to supply the secondary air into the mainstream. However, the secondary air will firstly go through the plenum chamber which is attached to the bottom side of the test duct parallel to slot position before it will be injected into the mainstream. To have the uniform flow to be injected, the screen is positioned inside the plenum chamber. A laminar flow meter was used to measure the mass flow rate of the secondary air.

Figure 18 illustrates the birdview of the test section. It consists of four parts: the inlet section, the blade section, secondary air inlet section for upstream leakage, and the outlet section. All components of the test section except the test cascade were made of acrylic-resin plate in order to keep visibility from outside. The inlet section is delimited by the hub

endwall, the tip endwall and the two side walls. Beneath the both side endwall an adjustable boundary layer bleed is employed to secure a parallel approaching flow field with a new boundary layer. An L-type miniature pitot tube was placed upstream of the model leading edge for inlet flow velocity measurement. The inlet velocity was about 16-18 m/s to meet desired inlet Reynolds Number. The blade section is a linear cascade consisted of 6 blades which had four identical HP turbine nozzle blades, and two dummy blades at outer side. The profile of the blade is shown in Table 1. The top view of test section and geometry of the leakage slot are shown in Figure 19. The upstream leakage slot was located at $-0.63C_{ax}$ upstream of the blade leading edge. The slot extended about 4 pitches and the width was $0.064C_{ax}$ (4mm). In consideration for the baseline condition, normal injection into the main flow was applied in this study. Second slot; segment gaps were located between the blade segments with opening about 1.75 mm. This slot extended from $x/C_{ax} = -0.63$ until $x/C_{ax} = 1.25$ with a curve slot near the blade throat. Behind the cascade, exit velocities of 50-60 m/s were obtained (Mach number approximately 0.15). The air is expanded to atmospheric pressure. Both of tailboard angle at cascade downstream were adjusted with gradually expanding passage in order to obtain the uniformity of inlet flow structures. The coordinate system is also presented in Figure 19 where X-axis is parallel to axial flow direction, Y-axis is parallel to pitchwise direction and Z-axis is parallel to spanwise direction. Figure 20 indicates the 3D CAD of the plenum chamber used in present study.

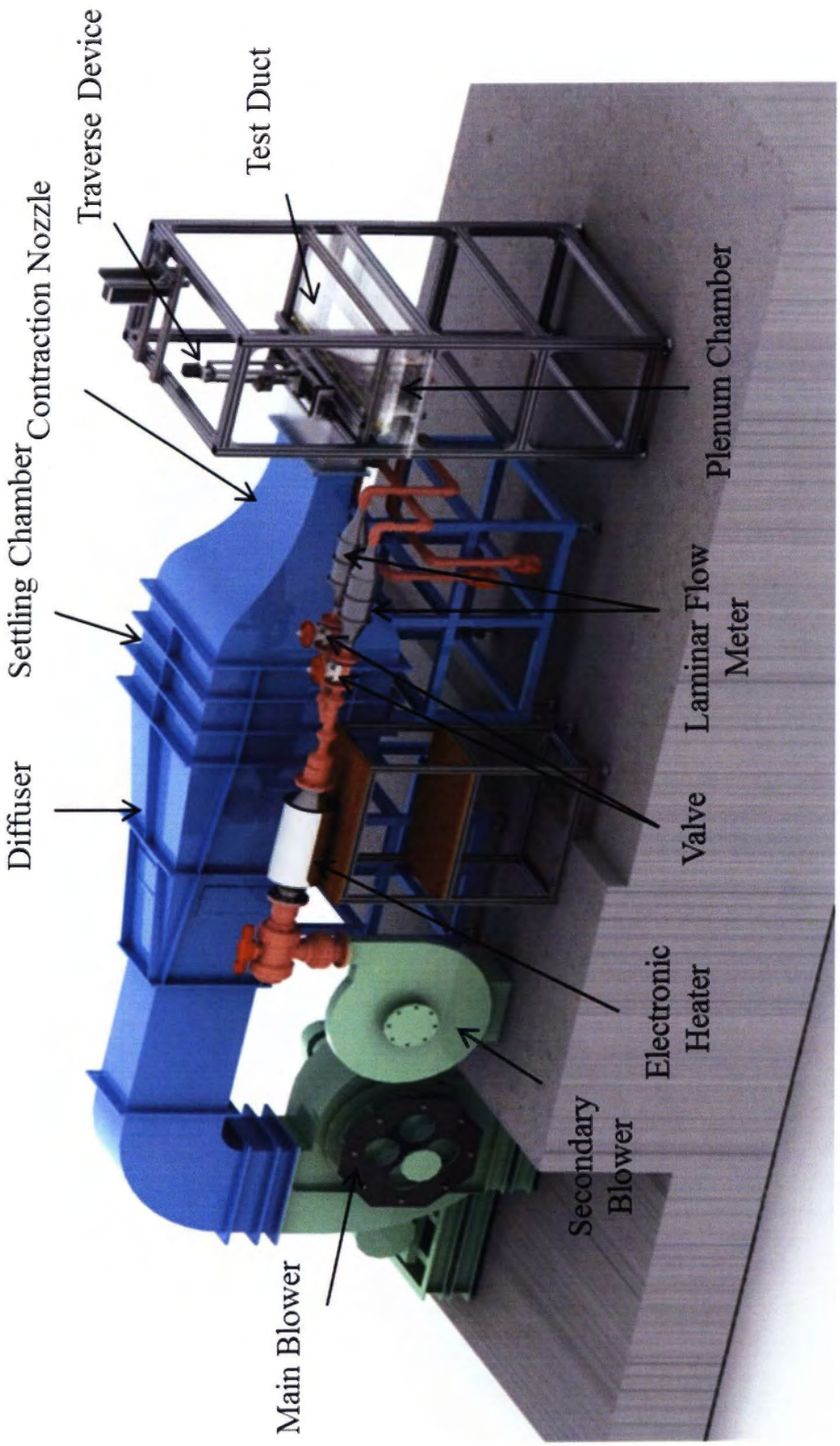

Figure 17 Schematic diagram of experimental facilities

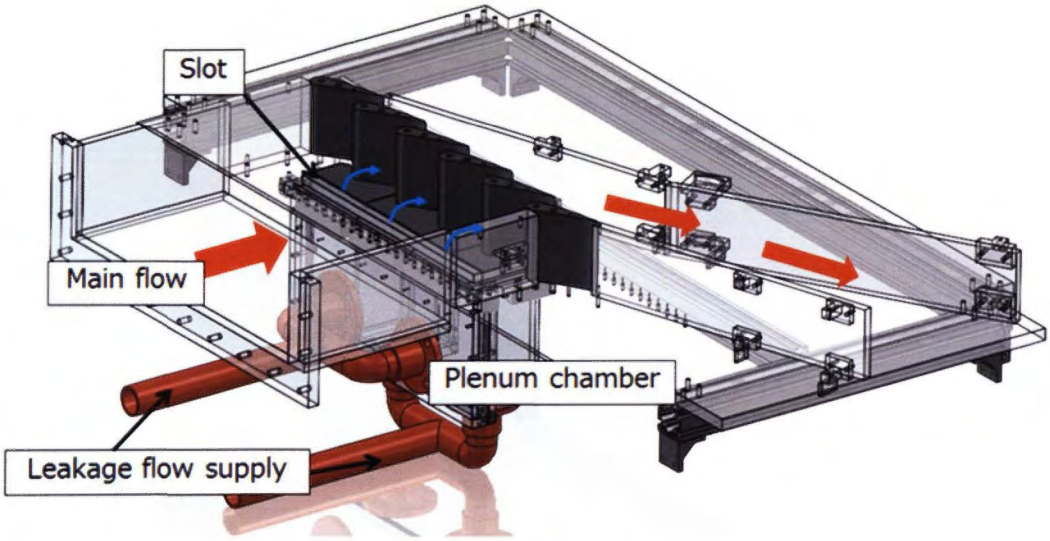

Figure 18 Birdview of the test duct

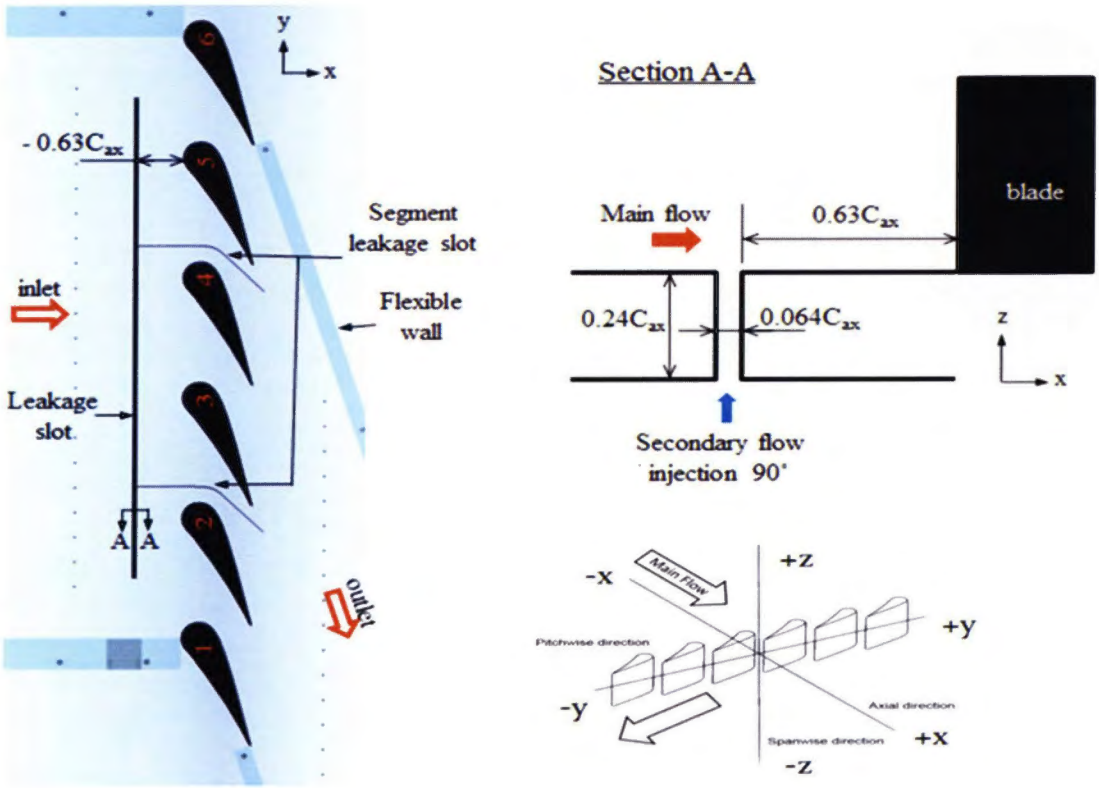

Figure 19 Overview of test duct

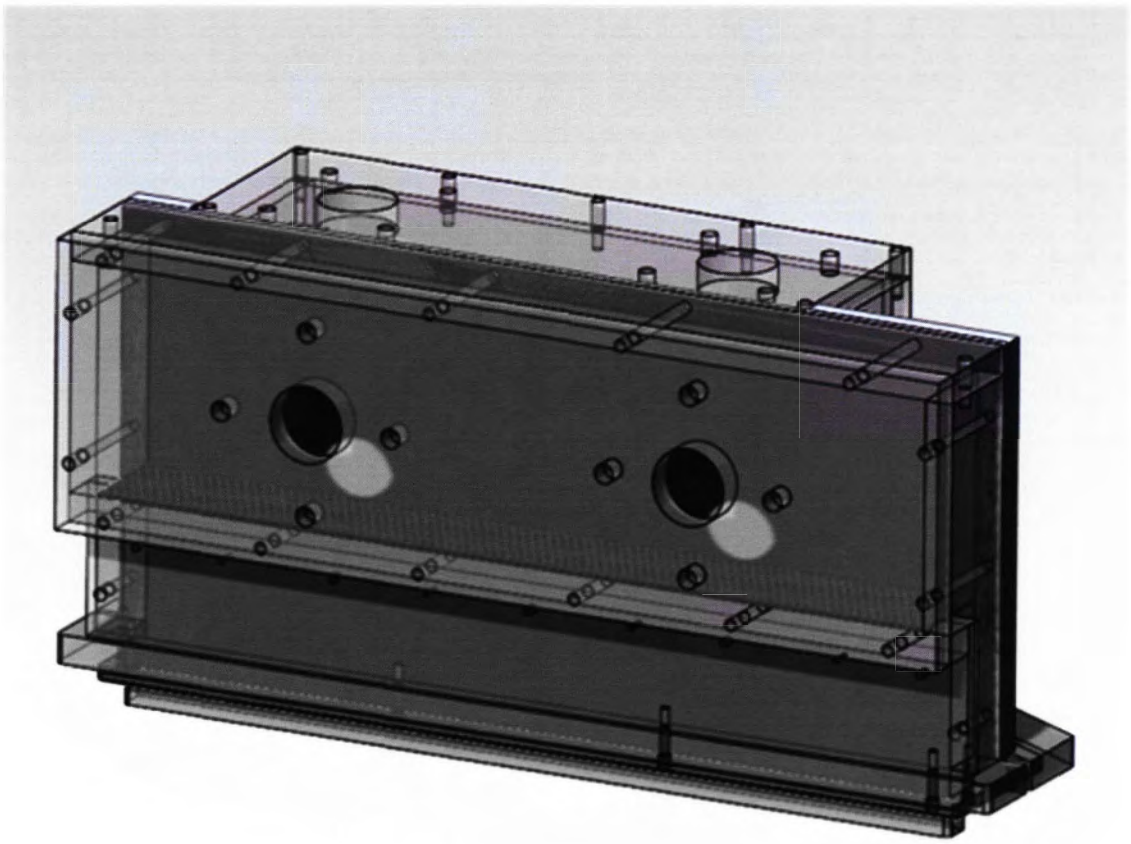

Figure 20 Plenum Chamber

2.3 Specification of measurement devices and laboratory equipment

The details of devices used are explained in the Table 2 below.

Table 2 Details of device and equipment

Device/equipment	Specifications
Main blower 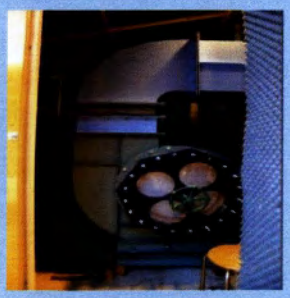	Manufacturer : MITSUYA FAN Model type : TVC No.4(Centrifugal type) Output : 18.5 kW Discharge flow rate : 320 m^3/min Discharge pressure : 200mmAq (20 ˚C) Rated speed : 2310rpm Outlet cross-sectional area : 400×500mm Rotation direction : clock-wise direction
Secondary blower 	Manufacturer : Okamoto Blower Model type : KO28-4 Output : 3.7 kW Discharge flow rate : 12 m^3/min Discharge pressure : 6.86 kPa (at 20℃) Speed : 2200 rpm
Laminar flow meter 	Manufacturer : Tsukasa Ken Measurement Model LFE-50B Rated flow 50 (l / s) F · S accurate to within ± 1.0% 0 ~ 80 (℃) use temperature range
Electric Heater 	Manufacturer: Kashima Co., Ltd. Model SR-9N Capacity: 13.5 (kW) Maximum wind speed 13.0 m^3/min

Pneumatic valve 	Manufacturer : CKD Co. Ltd Model type: AG31-01-2
Data logger (Aerodynamic measurement) 	Manufacturer : Nippon Electric Model : 7V14 Interface: RS232C
Data logger (Thermal measurement) 	National Instrument Model: DAQ-9174
Pressure transducer 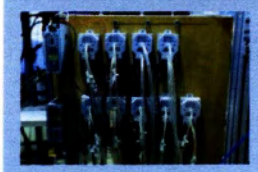	Manufacturer : Setra System Co. Ltd Model : 265 Measurement range: 0~5000 Pa accuracy±0.25%(±12.5 Pa)
Thermocouple 	Manufacturer : Suzuki Seiki K type
Black paint	Manufacturer : Nippon Capsule Product Type: SSM-8
Digital Thermometer 	Manufacturer: AND Model: AD-5624 (Auto-detect max/min temperature)

Thermo-chromic liquid crystal (TLC) 	Manufacturer : Nippon Capsule Product Type: RW24~26
Miniature pitot tube 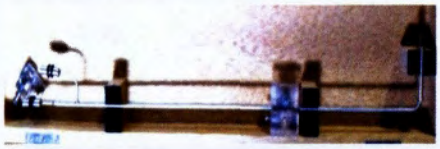	Manufacturer : Tsukubari Kaseiki L-type Outer diameter: 4mm Length: 60mm
5-holes pitot tube 	Manufacturer: Suzuki Seiki Arrow type Head diameter: 2.1mm Outer diamater: 9.5mm Length: 648mm
Personal computer 	OS: Window 7, 64 bit Processor: i7-2600, 3.4GHz HD drive: 500GB Memory: 8GB
Digital video camera 	Manufacturer: Sony Model type: CCD camera HDR-FX1000
Traverse device 	2-dimensional axis Pitchwise direction: max 600mm Spanwise direction: max 300mm precision: 0.1mm Motion Controller: PCI-7210C Motor Unit: UMK268B

Voltage adjustor 	Volt slider Manufacturer : YAMABISHI Model: S3P-240-30
Lamp 	Manufacturer : Toshiba Co. Ltd Type : Halogen lamp JDR110V60W/K5F

2.4 Test condition

All measurements have been conducted at fixed inlet Reynolds number based on inlet midspan velocity and the actual blade chord length, Re_{in}=125000. The definition of the Reynolds is given by Eq. (2)

$$\mathrm{Re}_{\infty} = \frac{\rho_{\infty} U_{\infty} C}{\mu} \tag{2}$$

where;

ρ_{∞}, mainstream air density [kg.m^{-3}];
U_{∞}, mainstream inlet velocity [m.s^{-1}];
C, actual blade chord [m]; and,
μ, mainstream air viscosity [kg.m^{-1}.s^{-1}]

The Reynolds number involved in the real gas turbine is far exceeding the considered value in the present study. Due to the limitations of the experimental setup, only such Reynolds number can be considered in the present study. In order to investigate the effect of the different amount of the leakage into the mainstream, which represented by mass flow ratio, MFR given by Eq. 3,

$$MFR = \frac{\dot{m}_2}{\dot{m}_{\infty}} \times 100 \tag{3}$$

Here,

$$\dot{m}_2 = \rho_2 Q_2 = \rho_2 A_2 U_2 \tag{3.1}$$

$$\dot{m}_{\infty} = \rho_{\infty} Q_{\infty} = \rho_{\infty} A_{\infty} U_{\infty} \tag{3.2}$$

Thus,

$$\dot{m}_2 = (1.2839 \times 10^{-4}) MFR \rho_{\infty} U_{\infty} n \tag{4}$$

where;

$\dot{m}_2$, secondary air mass flow rate, [kg/s];

$\dot{m}_\infty$, mainstream air mass flow rate, [kg/s];

Q_∞, mainstream air volume flow rate, [m^3/s];

Q_2, secondary air volume flow rate, [m^3/s];

U_∞, mainstream inlet velocity, [$m.s^{-1}$];

ρ_2, secondary air density, [$kg.m^{-3}$];

ρ_∞, mainstream air density, [$kg.m^{-3}$];

A, cross-sectional area for 1 pitch at inlet, (=0.012839 [m^2]); and

n, pitch number, [$kg.m^{-3}$].

In present study, in order to investigate the effect of the leakage and its potential to become as one of the cooling configuration, four mass flow ratio have been considered at MFR = 0.75%, 1.25%, 1.75% and 2.25%. These MFR have been selected by consideration of low, intermediate, higher and extremely higher leakage injection, respectively. The consideration of higher mass flow ratio was made due to the promising thermal results that have presented by the previous researcher. Furthermore, the potential of the leakage flow ejection as a cooling can be investigated and discussed.

2.5 Aerodynamics investigation

As shown in Figure 21, the measurement system is constituted by pneumatic 5-holes Pitot tube, traverse device, pressure transducer and data logger which are connected to the computer for data collection. The RS232 cable was used as interface transferring the measurement data from logger into the computer. Two measurement planes have been traversed in present study;

I. Inlet flow verification at plane $-0.85C_{ax}$
II. Outlet flow investigation at plane $1.25C_{ax}$

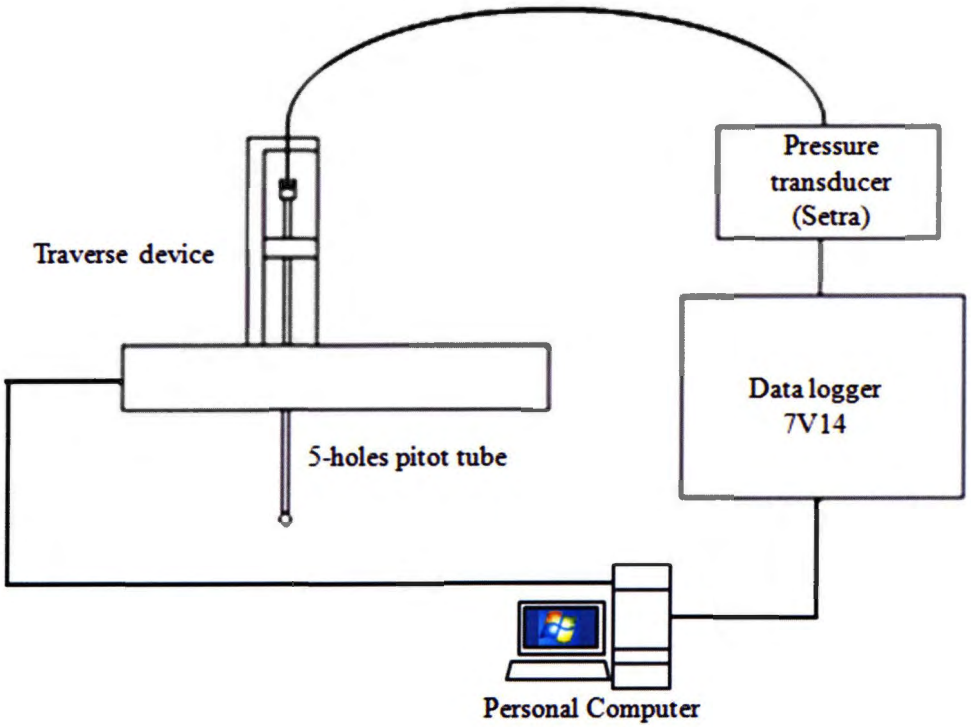

Figure 21 Data acquisition system

2.5.1 Inlet flow verification at plane -0.85C_{ax}

The locations of traverse planes are shown in Figure 22. The inlet flow field measurement has been conducted at the first in order to ensure uniform main flow structures entering the cascade. Pneumatic 5-holes Pitot tube measurements have been performed at -0.85C_{ax} upstream of blade leading edge, indicated by red dot-line in Figure 22. To conduct the measurement with fewer disturbances, the probe has been traversed along the region of blade 3 till blade 5 where they are located almost at the middle of the cascade. 5-holes pitot tube was fixed at 0° to ensure its properly measure the incoming flow within calibration range of -36° to 36°. Since the head diameter of probe was 2.1 mm, thus the nearest distance of measurement from the endwall could be positioned approximately 2 mm which means about 2% of the span direction. Figure 23 illustrates the measurement grid for 2.4 pitch to investigate the flow uniformity and periodicity. As shown in Figure 23, the probe was traversed for 25 in pitchwise direction and 18 in spanwise direction to provide 450 measurement points. The main flows Reynolds number of 1.25 x 10^5 was fixed throughout all test cases. The inlet Re was determined by measuring inlet flow velocity using miniature Pitot tube located at -1.85Cax.

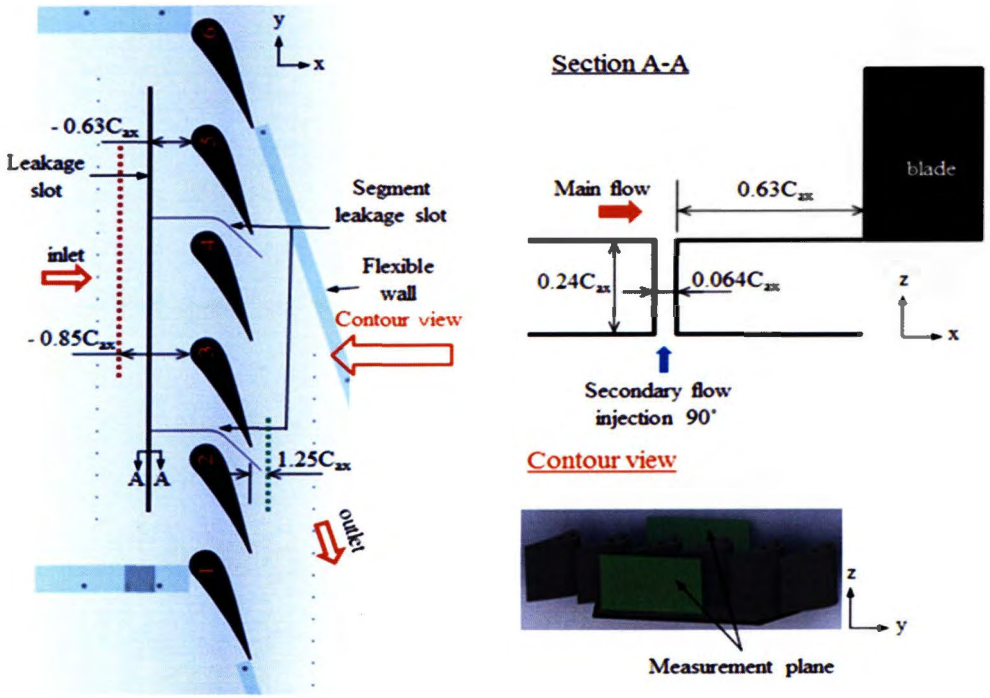

Figure 22 Aerodynamics measurement plane

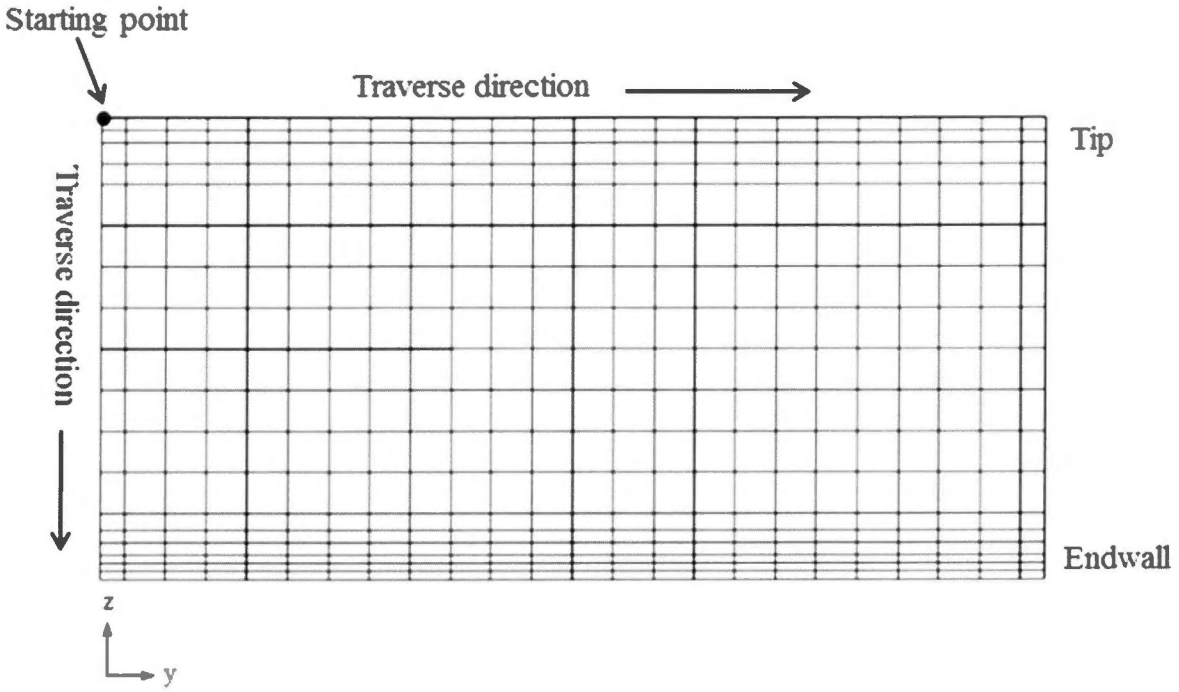

Figure 23 Measurement grid at inlet plane ($-0.85C_{ax}$)

2.5.2 Outlet flow investigation at plane $1.25C_{ax}$

The measurement was conducted at $1.25C_{ax}$ downstream of the blade LE which indicated by the green dot-line in Figure 22. In order to study the effect of the upstream leakage ejection included their injection amount, four MFR of 0.75%, 1.25%, 1.75% and 2.25% have been used in consideration on low, intermediate, high and extremely higher injection, respectively. The high and extremely high amount ejection were done in order to see the potential of the upstream leakage to work as cooling purpose thus their effect on the aerodynamics side also need to be revealed. However, the measurement without any leakage or secondary air injection was firstly carried out to observe a flow field of baseline condition at the same plane. This enables the direct comparison between baseline condition and leakage injection cases. For baseline condition case, a measurement was conducted without supplying a secondary air, therefore a flat endwall platform without slot was placed at the first to avoid a flow that coming from the high pressure mainstream moving into the slot which might be considered affecting the ongoing flow structures. The measurements at outlet plane were done by two phases where the first phase was to investigate a periodicity of flow at cascade outlet. 1600 points of measurement were started from the blade tip which traversing for 2

pitches and ended close to the endwall. On the other hand, second phase measurement were surveyed with a finer grid for only 1 pitch and a measurement started at midspan. The finest grid was 1 mm and coarsest was 10 mm with a 1148 points of measurement. Furthermore, the finer grid was adopted near the region where the blade wakes are expected. As shown in Figure 24, this plane has been surveyed by means of 28 traverses in the pitchwise direction, each of them constituted by 41 measuring points spaced with variable steps which have a finer grid near the endwall. For each measuring point 10 samples have been collected and the pressures were calculated as time-averaged components. However, results based on finer grid measurements only will be presented. As done for inlet measurement, the nearest distance of measurement from the endwall could be positioned approximately 2 mm which means the measurement range is approximately 2% to 50% of the span direction. Figure 22 indicates the viewpoint definition of all contours presented in this paper. Different case with inlet measurement, the probe was oriented to -72.3° of yaw angle for outlet flow measurement due to the flow turning at blade downstream. This angle was obtained based on the prediction using CFD simulation. The probe will not properly measure the total pressure at this plane by normal probe orientation as the flow deviation exceeding the maximum calibration range. Table 3 shows the flow conditions for each measurement.

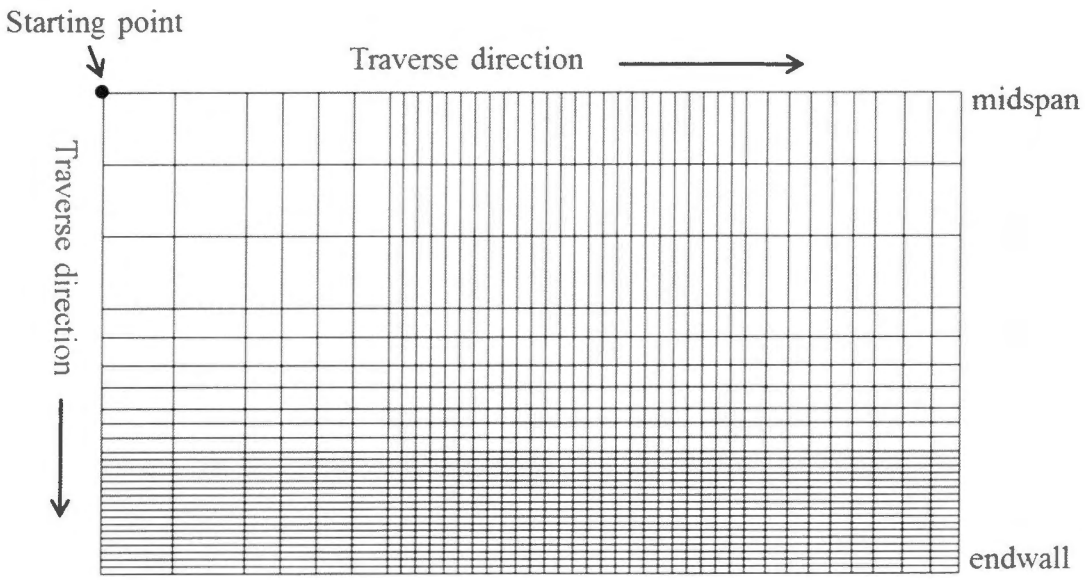

Figure 24 Measurement grid at outlet plane ($1.25C_{ax}$)

Table 3 Test flow condition

Parameter	MFR (%)				
	baseline	0.75	1.25	1.75	2.25
Re_∞	1.25×10^5				
$P_{t\infty}$[Pa]	1584	1749	1752	1662	1700
T_∞[°C]	33	36	37	34	40
T_2 [°C]		47	48	48	47
U_∞[m/s]	17.1	17.7	17.6	17.4	17.3

2.5.3 Data reduction

The flow measurement by conducting 5-holes pitot tubes enables the investigation of 3-dimensional flow structures at cascade downstream. Figure 25 illustrates the definition of the 5-holes Pitot tube to describe the yaw and pitch angle. The flow yaw angle, α and pitch angle, σ can be determined by applying 3 components of velocities measured by the 5-holes Pitot tube as shown in Eq. 5 and Eq. 6

Yaw angle : $$\alpha = \frac{180}{\pi} \times \tan^{-1}\left(\frac{v}{u}\right) \quad (5)$$

Pitch angle : $$\sigma = \frac{180}{\pi} \times \tan^{-1}\left(\frac{w}{u}\right) \quad (6)$$

where,

u, pitchwise direction velocity component [m/s]

v, spanwise direction velocity component [m/s]

w, axial direction velocity component [m/s]

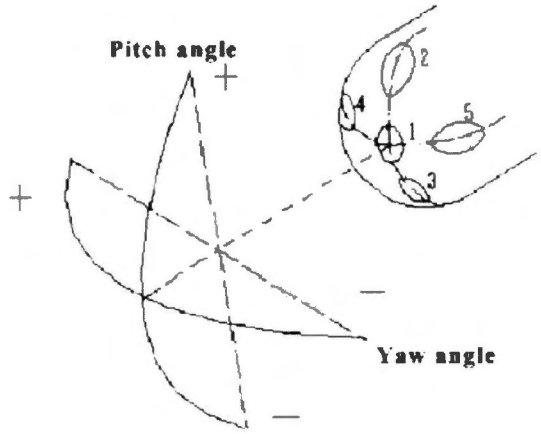

Figure 25 5-holes Pitot tube definition

The local total pressure obtained from the measurement along the plane also has been use to describe the aerodynamics performance of the test cascade by determine the total pressure loss coefficient, C_{pt} as presented in Eq. 7. Total pressure loss also can be defined as Eq. 8.

$$C_{pt,1} = \frac{P_{t,\infty} - P_{t,out}}{\frac{1}{2}\rho U_{\infty}^2} \tag{7}$$

$$C_{pt,2} = \frac{P_{t,ref} - P_{t,out}}{\frac{1}{2}\rho U_{\infty}^2} \tag{8}$$

Here,

$$P_{t,ref} = \frac{\dot{m}_2}{\dot{m}_2 + \dot{m}_{\infty}} P_{t,2} + \frac{\dot{m}_{\infty}}{\dot{m}_2 + \dot{m}_{\infty}} P_{t,\infty} \tag{8.1}$$

Note that the effect of the secondary air from the plenum chamber is neglected in Eq. 7 while it is taken into account in Eq. 8 by considering the total pressure inside the plenum chamber.

However, Eq. 7 has been used in present study due to the difficulty to measure the total pressure inside the plenum chamber within a very limited space. However, prediction presented that the different between these two equations was less than 1% and could be neglected. The vorticity, ζ as a rate of flow rotation in 2-dimensional plane (axis y and z) has been determined in order to reveal the flow behavior at those planes as defined by Eq. 9.

$$\zeta = \frac{\partial w}{\partial y} - \frac{\partial v}{\partial z} \tag{9}$$

Both C_{pt} and ζ contours presented by the experimental will be compared with the numerical simulation for validation which enables the more accurate prediction of flow structures in the blade passage. Finally, secondary kinetic energy coefficient, C_{SKE} as been shown in Eq. 10 was also determined for a details discussion on the flow behavior.

$$C_{SKE} = \frac{SKE}{\frac{1}{2}\rho U_{out,mid}^2} \tag{10}$$

Here,

$$SKE = \frac{1}{2}(V_{\sec}^2 + W_{\sec}^2) \tag{10.1}$$

$$V_{\sec}^2 = \left(u\sin(\alpha_{out,mid}) - v\cos(\alpha_{out,mid})\right)^2 \tag{10.2}$$

$$W_{\sec}^2 = w^2 \tag{10.3}$$

In the mean endwall flow field, the rotational energy at the endwall is typically quantified by the magnitude of SKE. Using averaged exit flow angle at midspan as the primary reference direction, SKE is defined as half the sum of squared mean velocity component normal to the primary reference. SKE then be normalized with the dynamics pressure to determine the C_{SKE}.

2.6 Thermal investigation

2.6.1 *Thermo-chromic* liquid crystal (TLC)

The development of *thermo-chromic* liquid crystal (TLC) based thermography over the past 30 years has provided thermal engineers with a relatively in expensive technique for visualizing and measuring surface temperature. TLC is temperature indicators that modify incident white light and display color whose wavelength is proportional to temperature. *Thermo* is refers to temperature while *chromic* refers to color. They can be painted on a surface or suspended in the fluid and used to make visible the distribution of temperature. The displayed color is red at the low temperature margin and blue at the high end. The color changes smoothly from red to blue as a function of temperature. The chemical makeup of TLC material fixes its color-temperature response at the time of manufacture. A simple, two color/temperature design at or typically describes this response and can be useful in qualitative applications and for properly selecting a TLC formulation for a particular application. Engineers and scientist have successfully used TLC thermography to investigate various thermal phenomena in wide variety of applications. These applications include gas turbine heat transfer. In present study, RW24-26 of TLC has been used to describe that the color changes occurs at temperature range of 24°C to 26°C. In order to observe the color change due to the temperature different, the mainstream temperature must be below 24°C while the secondary air temperature should be higher than this range.

2.6.2 Temperature measurement by TLC

Thermal investigation was conducted by the same wind tunnel used for the aerodynamics investigation. However, some modifications on the test section have been done in order to obtain high accuracy of the measurement. As illustrates in Figure 26, the endwall side of the test section included the blades were black painted in order to reduce the light reflection towards camera during the measurement. To have a clear visualization on the endwall side from the top, the tip side wall of the cascade has been replaced with a flat and clean acrylic plate. Figure 26 also indicates the region of the temperature measurement which was focuses on the endwall region between blade 3 and blade 4. Figure 27 shows two configurations of TLC coating for the measurement. As shown in the figure 27, an acrylic plate was firstly painted by a black color then the TLC layer was coated for configuration A

while the TLC layer was firstly coated then follows by the black panting. This configuration is actually depending on the camera position. In present study, configuration A was adopted since the temperature changes on the endwall was captured from the tip side of test section. This means the camera will be positioned from the top side of test section. Thus, the TLC layer must be coated on black painted acrylic plate in order to keep the visibility during the measurement. Figure 28 illustrates how the measurement was carried out, including camera and light positions. The color change of the TLC was recorded with a digital video camera, and recorded image data were captured by PC frame by frame, then converted from RGB images into HSL (Hue/Saturation/Lightness) images using a software (GraphicsConverter)(Hachiya, 2004). The accuracy of the measurement techniques was based on Funazaki [30].

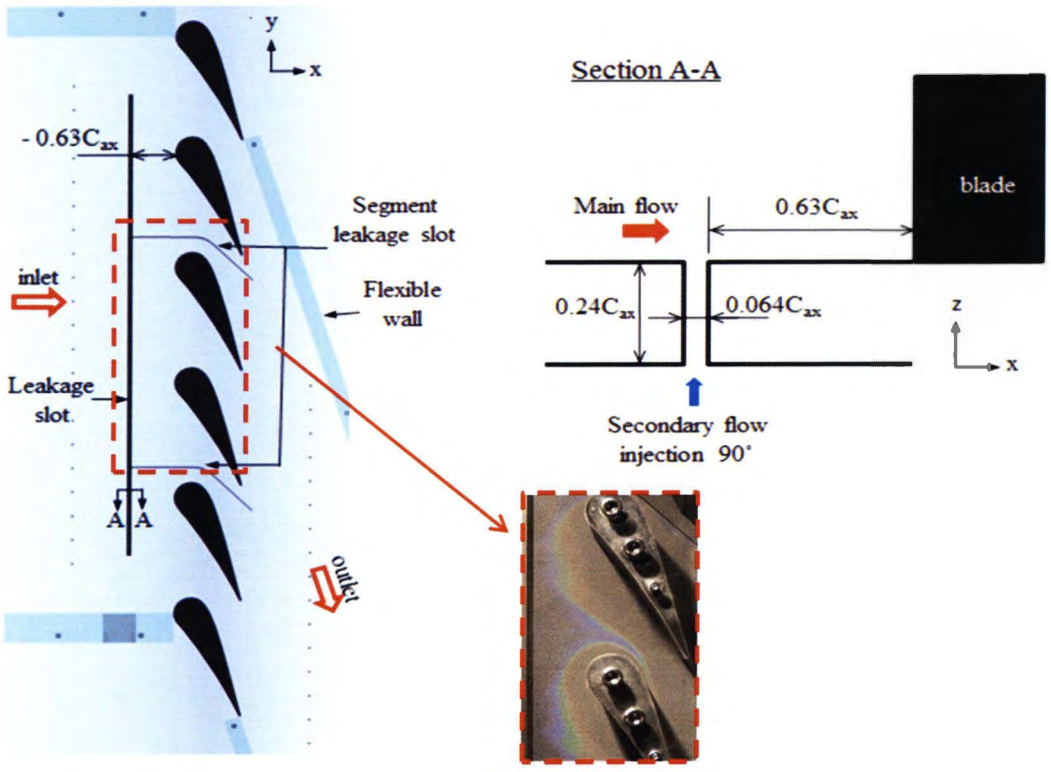

Figure 26 Temperature measurement region

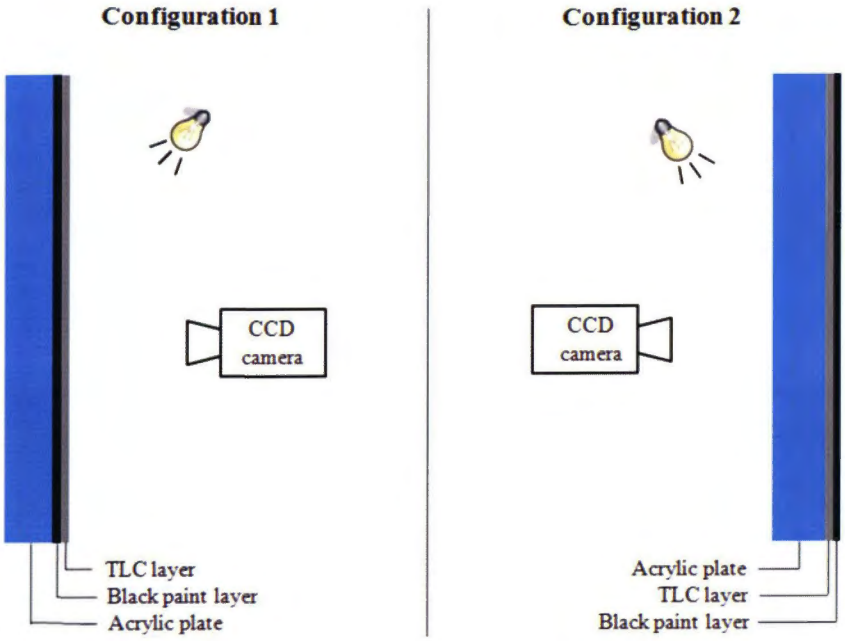

Figure 27 TLC coating configurations

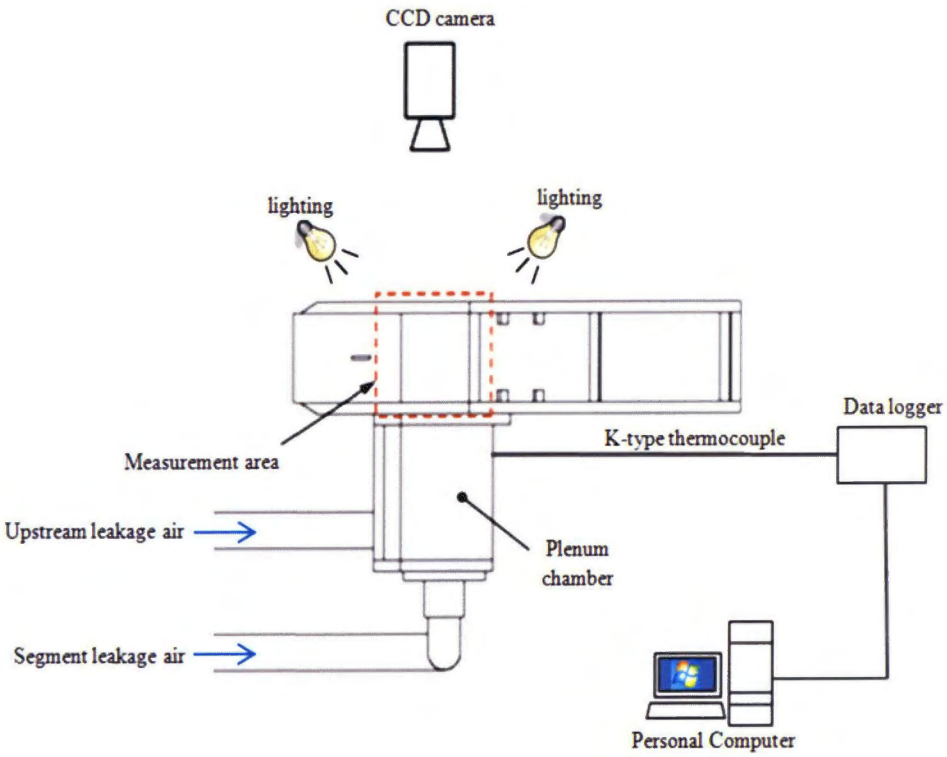

Figure 28 Temperature measurement system

2.6.3 TLC calibration

The relationship between the temperature and measured Hue of the reflected light defines the calibration curve for the TLC. Figure 29 shows the calibration device that was used where the stainless sheet was attached on the acrylic plate with two cooper electrodes were fixed at the end. The TLC was coated onto the stainless sheet surface by configuration A to have a similar condition with the measurement. The voltage was applied through the electrodes and the color changes due the temperature different on the calibration plate were captured by the same camera used in the measurement. At the same time, the temperature distribution was measured by sixteen K-type thermocouples which were attached on the bottom side of the plate. In order to reduce the uncertainties, the calibration test was conducted in place in the wind tunnel with the same lighting level and viewing angle used during the data acquisition phase of the measurement as shown in Figure 30. The RGB images captured during the calibration test which was converted to HSL images is shown in Figure 31. Then, Eq. 11 was used to obtain the relationship between temperature and Hue

$$\frac{T_s - T_L}{P_s - P_L} \times (P - P_L) + T_L \tag{11}$$

where,

P, Hue value at specified pixel position;

P_S, Pixel position of the low-temperature side thermocouple;

P_L, Pixel position of the high-temperature side thermocouple;

T_S, low side temperature measured at P_S; and

T_L, high side temperature measured at P_L.

Finally, the curve can be plotted as shown in Figure 32. Based on the Figure 32, the Hue range of 30~170 illustrating the most accurate characteristic has been selected for the data post-processing purpose.

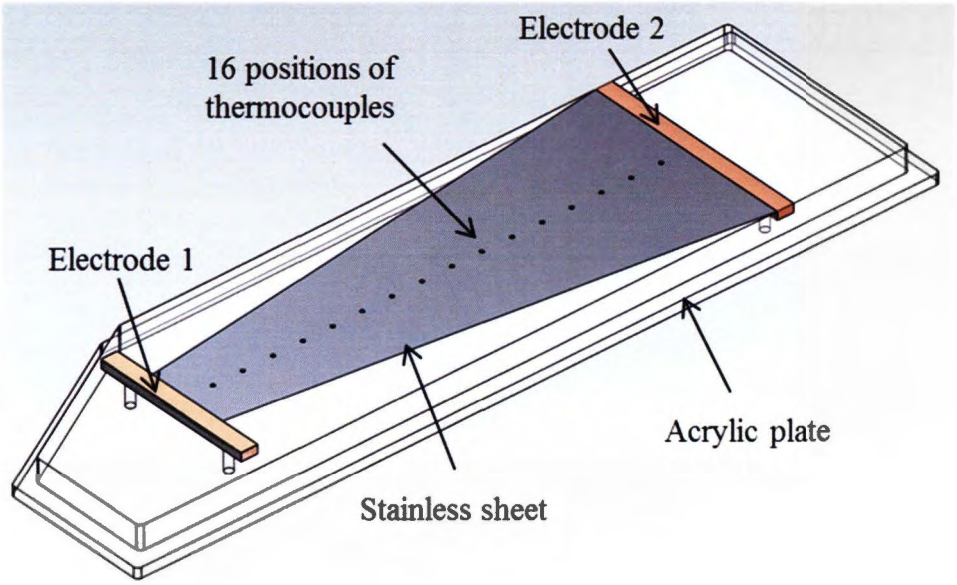

(a) Schematic view TLC calibration plate

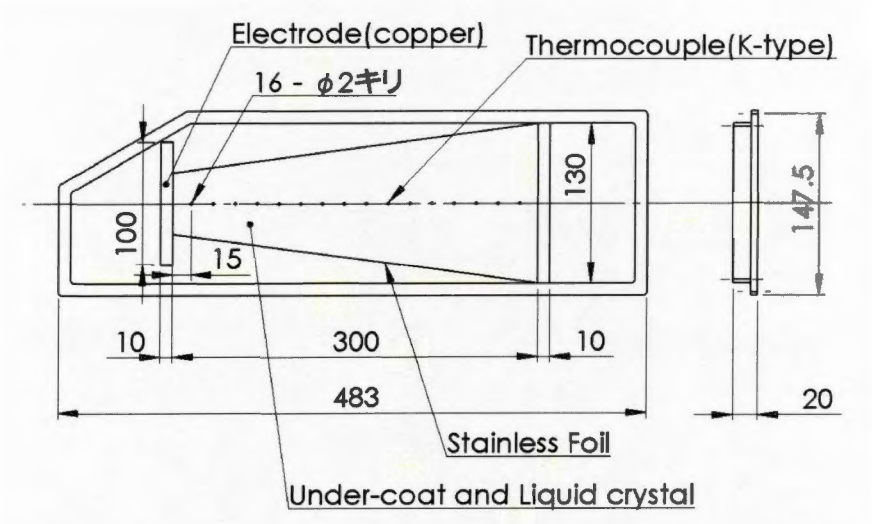

(b) TLC calibration plate with dimension

Figure 29 TLC calibration plate

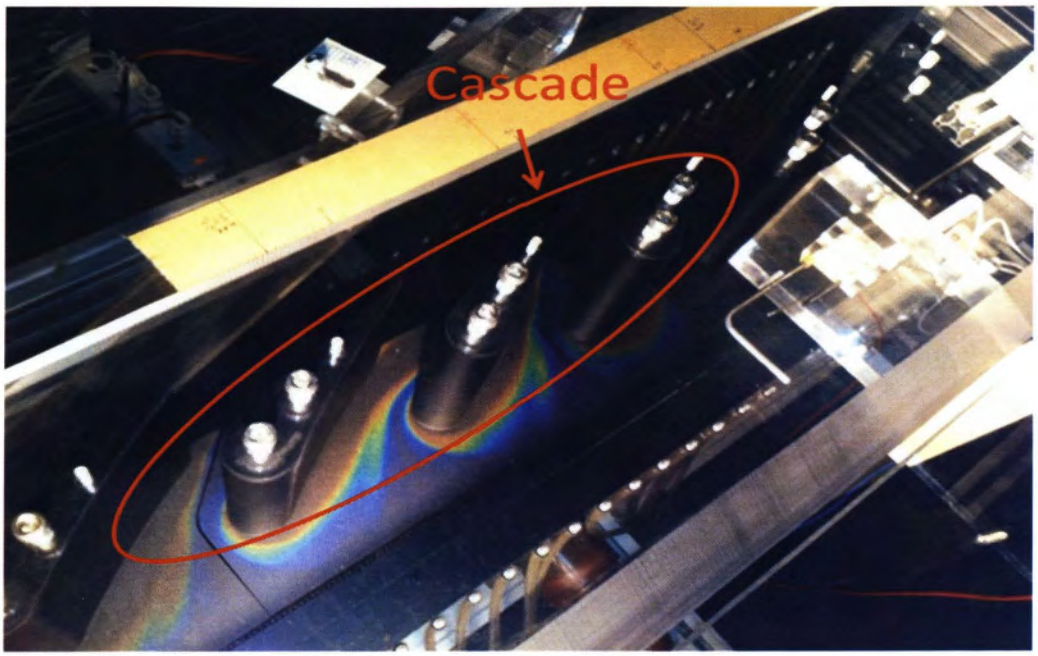

(a) Actual measurement

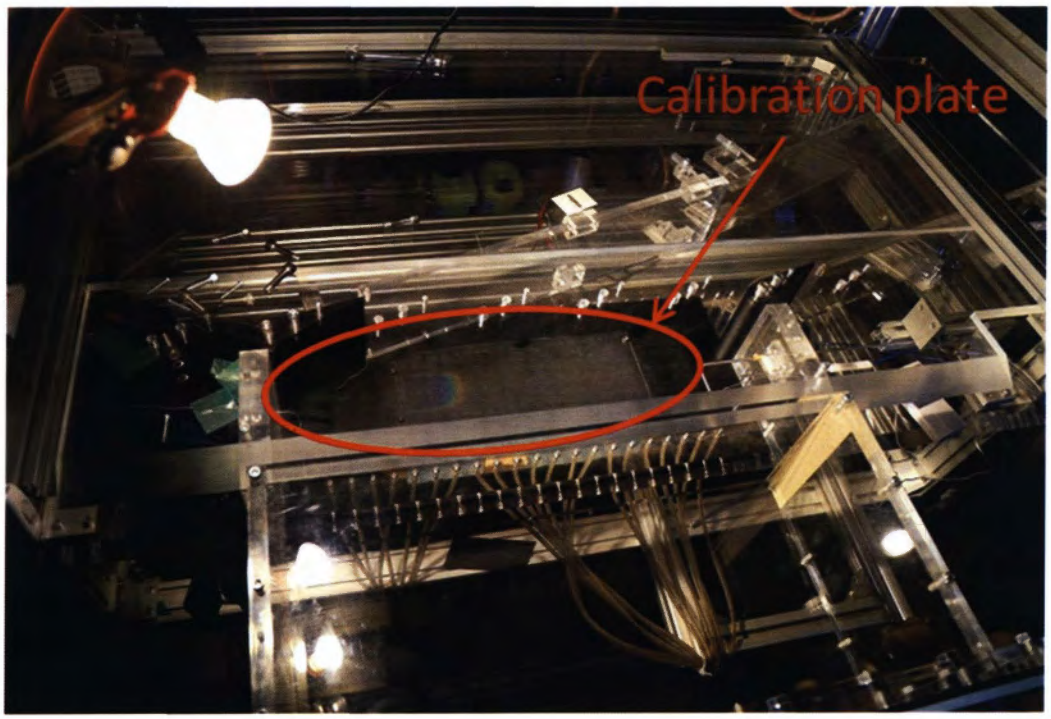

(b) Calibration test

Figure 30 Position of calibration plate during test

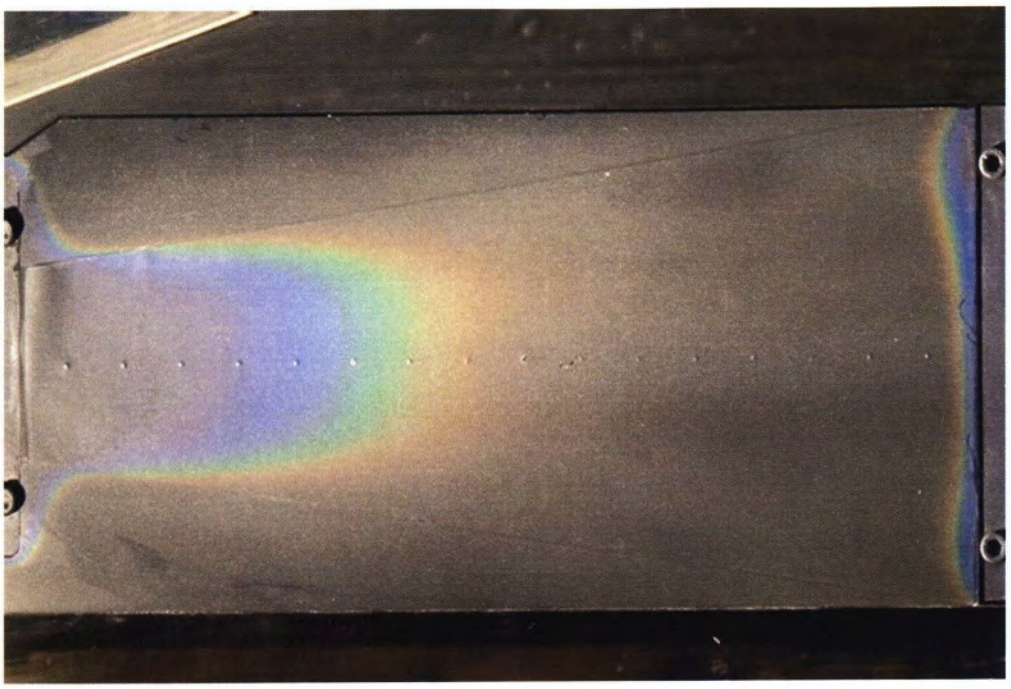

(a) RGB image

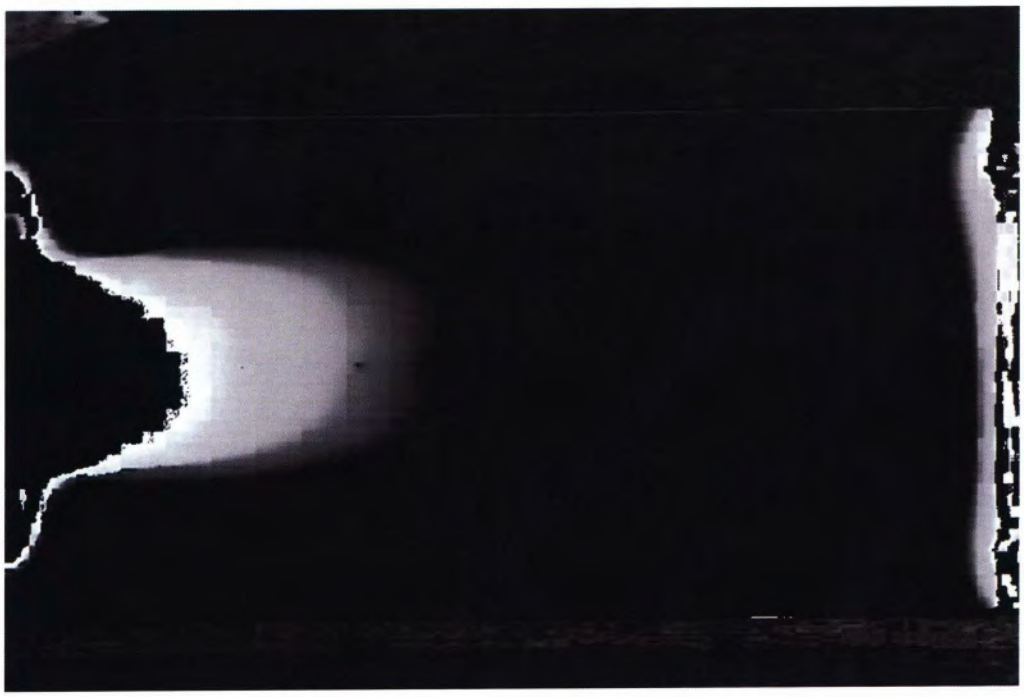

(b) Hue image

Figure 31 RGB image (a) converted to HUE image (b)

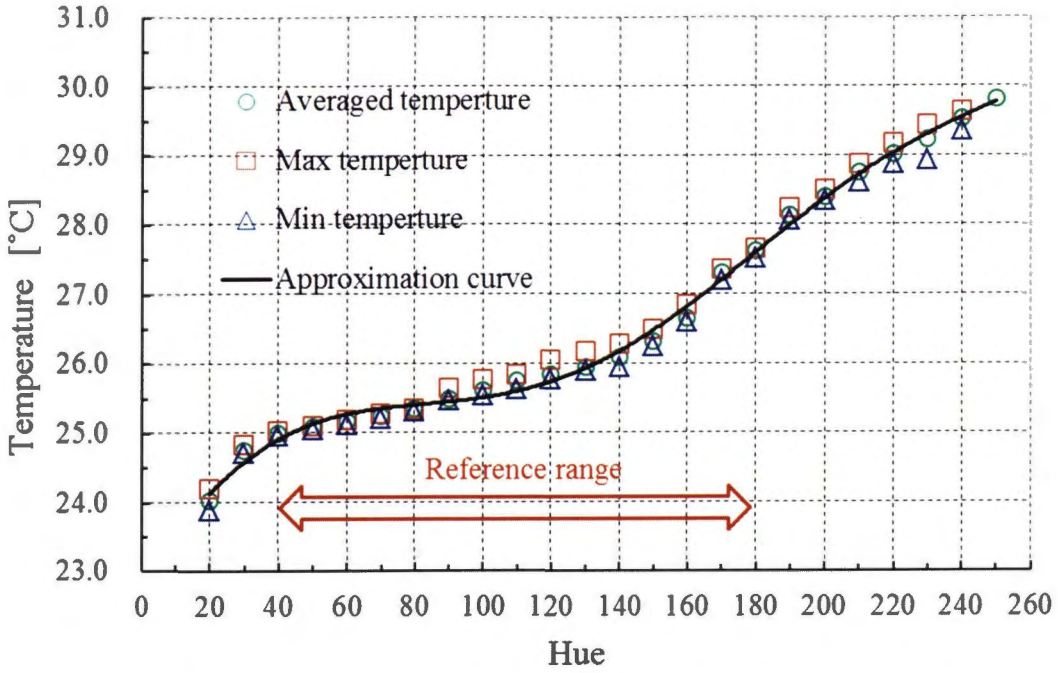

Figure 32 TLC calibration curve

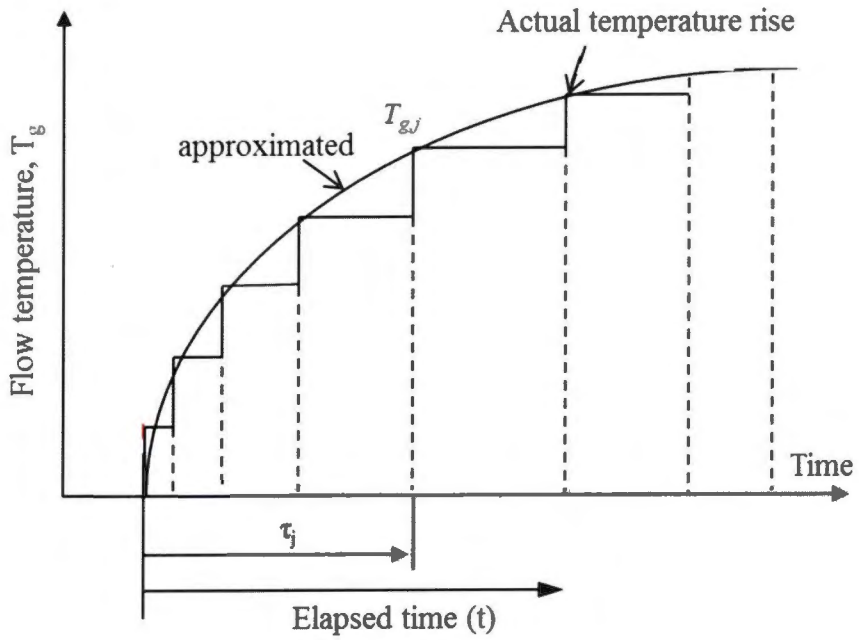

Figure 33 Temperature rise curve by step series of temperature gradual

2.6.4 Transient method

This study employed a transient method to determine heat transfer coefficient and film effectiveness from the time-varying temperature data of the surface. A brief description on the method is given in the following. Temporal change of the surface temperature on semi-infinite body T_w subjected to step-like temperature change of the flow over the body with constant heat transfer coefficient, h is provided from the solution of one-dimensional heat conduction equation as

$$\frac{T_w - T_i}{T_g - T_i} = 1 - \exp\left(\frac{h^2 t}{\rho c \lambda}\right) erfc\left(\frac{h\sqrt{t}}{\sqrt{\rho c \lambda}}\right). \tag{12}$$

Where,

T_i, initial temperature of the body;

T_g, flow temperature;

ρ, density;

c, specific heat; and

λ, thermal conductivity.

In a real situation, since it is almost impossible to obtain a step-like temperature rise of the flow, as shown in Figure 33, Duhamel's theory can be applied to cope with a gradual temperature rise. In this case the temperature rise is approximated by a series of steps with small temperature increase, which yields the expression for the time-varying wall temperature as

$$T_w(t) - T_i = \sum_{j=1}^{N} U(t - \tau_j)(T_{g,j} - T_{g,j-1}) \tag{13}$$

Here,

$$U(t - \tau_j) = 1 - \exp\left\{\frac{h^2(t - \tau_j)}{\rho c \lambda}\right\} erfc\left\{\frac{h\sqrt{t - \tau_j}}{\sqrt{\rho c \lambda}}\right\} \tag{13.1}$$

When applying the above-mentioned relationship to film cooling situation, the flow

temperature T_g in Eq. 13 should be replaced by adiabatic wall temperature, T_{aw}. Since film cooling effectiveness η is defined as,

$$\eta = \frac{T_{aw} - T_\infty}{T_2 - T_\infty} \tag{14}$$

where T_∞ and T_2 are main and secondary flow temperatures. The adiabatic wall temperature can be written by

$$T_{aw} = \eta T_2 + (1-\eta)T_\infty \tag{15}$$

Suppose that the film effectiveness remains constant even when the temperature rise of the secondary flow is approximated by a series of step-like temperature change, the following expression can be used for T_{aw}

$$T_{aw,j} = \eta T_{2,j} + (1-\eta)T_\infty \tag{16}$$

Therefore, Eq. (13) can be rewritten by substituting Eq. (17) into $T_{g,j}$

$$T_w(t) - T_i = \eta \sum_{j=1}^{N} U(t-\tau_j)t_{2,j} - \tau_{2,j-1}) \tag{17}$$

Eq. 17 can be regarded as a non-linear equation with respect to two variables, i.e., film effectiveness, η and heat transfer coefficient h. Combination of two different wall temperatures for two different elapsed times t_a and t_b given by Eq. 17 yield

$$\frac{T_w(t_a) - T_i}{T_w(t_b) - T_i} = \frac{\sum_{j=1}^{N} U(t_a - \tau_j)(T_{2,j} - T_{2,j-1})}{\sum_{j=1}^{N} U(t_b - \tau_j)(T_{2,j} - T_{2,j-1})} \tag{18}$$

This is an equation only with respect to h, from which h can be determined by solving Eq. 18 numerically. Then, film effectiveness can be given as follows,

$$\eta = \frac{T_w(t_a) - T_i}{\sum_{j=1}^{N} U(t_a - \tau_j)(T_{2,j} - T_{2,j-1})} \tag{19}$$

However, there are required several procedures before the h and η can be properly calculated by this method. Figure 34 illustrates the procedures of overall data post processing.

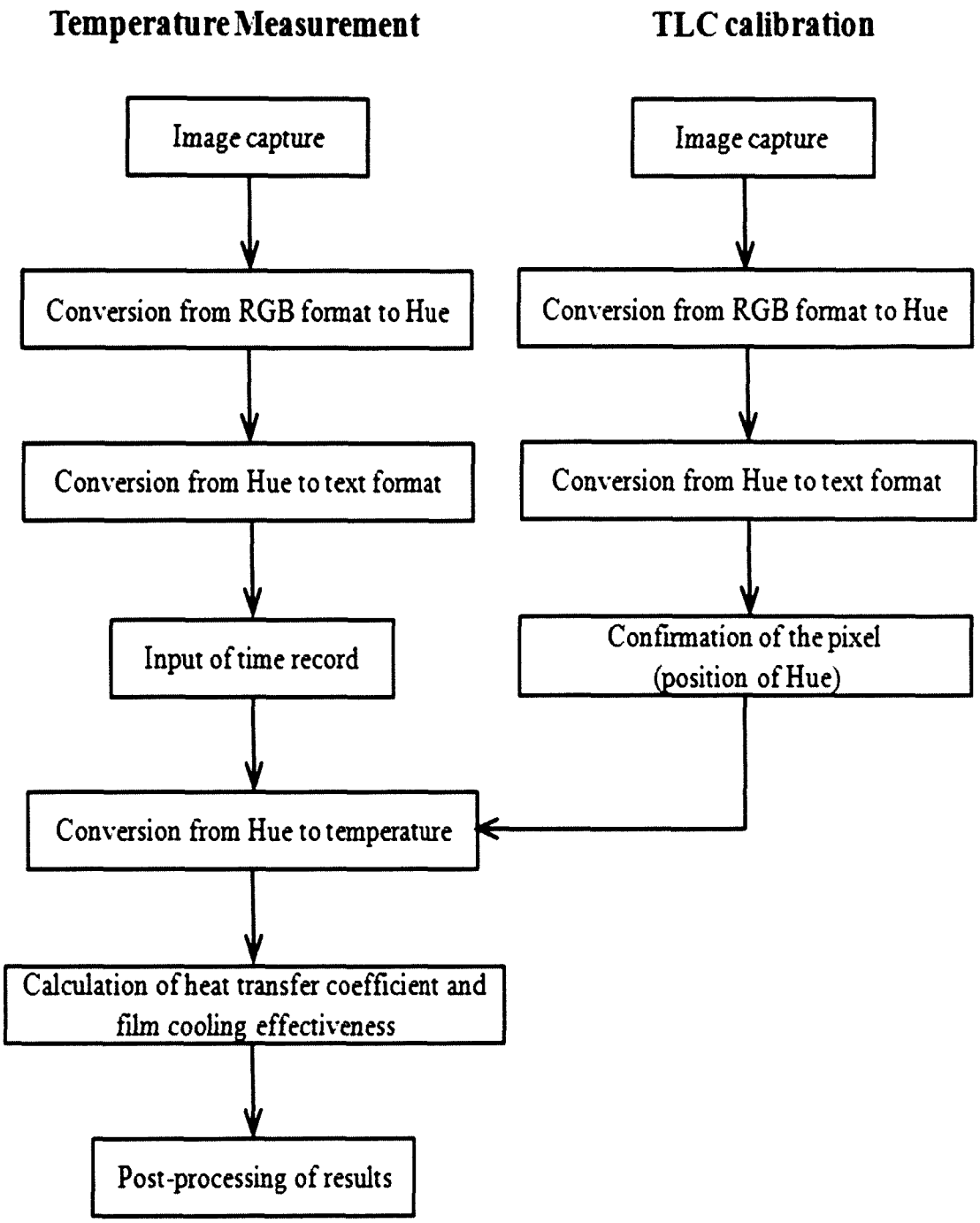

Figure 34 Data post processing procedures

2.7 Experimental uncertainty

2.7.1 Uncertainty definition

Experimental uncertainty analysis is important to evaluate the level of confidence in the results. Uncertainty analysis is a powerful tool for improving the value of experimental work, and can be applied during all phases of an experimental program. The greatest value of uncertainty analysis is almost certainly obtained when it is used during the planning of an experiment, Kline [31]. The general case of an experimental result, R, computed from j measured variables $X_{1...j}$, the data reduction equation is:

$$R = f(X_1, X_2, X_3 .....X_j) \tag{20}$$

and the uncertainty in the experimental result is given by

$$\left(\frac{U_R(R)}{R}\right)^2 = \left(\frac{U_{X_1}(X_1)}{X_1}\right)^2 + \left(\frac{U_{X_2}(X_2)}{X_2}\right)^2 + \left(\frac{U_{X_3}(X_3)}{X_3}\right)^2 + ... + \left(\frac{U_{X_j}(X_j)}{X_j}\right)^2 \tag{21}$$

Here,

$$\left(\frac{U_{X_n}(X_n)}{X_n}\right) = \delta_D + \varepsilon \quad (n = 1, 2, 3, ...j) \tag{22}$$

Where,

U_R uncertainty in the result,

U_{Xn}, uncertainty in the variable X_n

δ_D, device accuracy uncertainty

ε, standard deviation

This is the most general form of the uncertainty propagation equation, Coleman and Steele [32]. The uncertainty due to device accuracy, δ_D and the standard deviation, ε can be determined by Eq. 23 and Eq. 24, respectively.

$$\delta = \frac{D_{acc}}{\sqrt{3}} \tag{23}$$

$$\varepsilon = \frac{\frac{X_{n,Max} - X_{n,Min}}{2\sqrt{3}}}{X_{n,Average}} \tag{24}$$

Where,

D_{acc}, accuracy of the measurement device

$X_{n,Max}$, maximum value of X_n

$X_{n,Min}$, minimum value of X_n

$X_{n,Average}$, average of X_n

The overall experimental uncertainty can be calculated by determine the root square of Eq. 21. The details of the experimental uncertainties also presented by Moffat [33] and Alok [34].

2.7.2 Aerodynamic measurement uncertainties

In present study, the accuracy of the measurement device is also considered in the calculation. For instant, the uncertainty of the pressure transducer approximately ±1% (Setra 265: 0~5000Pa) is considered as one of the variable. The procedure to determine the uncertainty of the total pressure loss is explained below. Based on Eq. 7, C_{pt} is dependent on three variables; inlet total pressure, $P_{t,\infty}$, outlet total pressure, $P_{t,out}$ and dynamic pressure, P_d. By considering

$$P_{loss} = P_{t,\infty} - P_{t,out} \tag{25}$$

Thus, based on Eq. 21, the uncertainty of the total pressure loss can be determined by Eq. 26

$$\left(\frac{U(C_{pt})}{C_{pt}}\right)^2 = \left(\frac{U(P_{loss})}{P_{loss}}\right)^2 + \left(\frac{U(P_d)}{P_d}\right)^2 \tag{26}$$

Here,

$$\left(\frac{U(P_{loss})}{P_{loss}}\right)^2 = \left(\frac{U(P_{t,\infty})}{P_{t,\infty}}\right)^2 + \left(\frac{U(P_{t,out})}{P_{t,out}}\right)^2 \tag{26.1}$$

Based on Eq. 22, Eq. 23 and Eq. 24,

$$\left(\frac{U(P_{t,\infty})}{P_{t,\infty}}\right) = \frac{D_{acc,tran}}{\sqrt{3}} + \frac{\frac{P_{t,\infty,Max} - P_{t,\infty,Min}}{2\sqrt{3}}}{P_{t,\infty,Average}} \tag{26.2}$$

$$\left(\frac{U(P_{t,out})}{P_{t,out}}\right) = \frac{D_{acc,tran}}{\sqrt{3}} + \frac{\frac{P_{t,out,Max} - P_{t,out,Min}}{2\sqrt{3}}}{P_{t,out,Average}} \tag{26.3}$$

$$\left(\frac{U(P_{d})}{P_{d}}\right) = \frac{D_{acc,tran}}{\sqrt{3}} + \frac{\frac{P_{d,Max} - P_{d,Min}}{2\sqrt{3}}}{P_{d,Average}} \tag{26.4}$$

Where,

$D_{acc,tran.}$ accuracy of the pressure transducer (Setra 265)

$P_{t,\infty,Max}$, maximum value of inlet total pressure

$P_{t,out,Max}$, maximum value of outlet total pressure

$P_{d,Max}$, maximum value of inlet dynamic pressure

$P_{t,\infty,Max}$, minimum value of inlet total pressure

$P_{t,out,Max}$, minimum value of outlet total pressure

$P_{d,Max}$, minimum value of inlet dynamic pressure

$P_{t,\infty,Average}$, average of inlet total pressure

$P_{t,out,Average}$, average of outlet total pressure

$P_{d,Average}$, average of inlet dynamic pressure

Thus, the overall experimental uncertainty can be defined by Eq. 27 by substituting Eq. 26.1, Eq. 26.2, Eq. 26.3 and Eq. 26.4 into Eq. 26

$$\left(\frac{U(C_{pt})}{C_{pt}}\right) = \sqrt{\left(\frac{U(P_{loss})}{P_{loss}}\right)^2 + \left(\frac{U(P_{d})}{P_{d}}\right)^2} \tag{27}$$

In present study, the uncertainty for the MFR was also determined by the same procedures. The uncertainties analysis results for C_{pt} and MFR is shown in Table 4. The dynamics pressure is the variable which was highly influenced the uncertainty during the measurement.

Table 4 Experimental uncertainties analysis for aerodynamics

Uncertainty	Baseline	MFR= 0.75%	MFR= 1.25%	MFR= 1.75%	MFR= 2.25%
C_{pt} (%)	±3.54	±3.34	±2.57	±2.96	±2.79
MFR	±2.54	±4.72	±4.55	±3.79	±3.12

2.7.3 Thermal measurement uncertainties

The thermal measurement was conducted based on the transient method by applying one-dimensional heat conduction equation as shown in Eq. 12. Based on the post processing procedures, the heat transfer coefficient, h was firstly determined follows by film cooling effectiveness, η. This means that η contour depends on h. Hence, the uncertainty of h will firstly determine then be included as one of the variable for η uncertainty analysis. From Eq. 12 and Eq. 21, the uncertainty for h is shown in Eq. 28.

$$\left(\frac{U(h)}{h}\right)^2 = \left(\frac{U(T_2 - T_\infty)}{T_2 - T_\infty}\right)^2 + \left(\frac{U(T_w - T_\infty)}{T_w - T_\infty}\right)^2 + \left(\frac{U(t)}{t}\right)^2 + \left(\frac{U(\lambda)}{\lambda}\right)^2 + \left(\frac{U(c)}{c}\right)^2 \quad (28)$$

Since the same equation was used to determine η, thus its uncertainty can be defined as Eq. 29 where the h uncertainty is also included.

$$\left(\frac{U(\eta)}{\eta}\right)^2 = \left(\frac{U(h)}{h}\right)^2 + \left(\frac{U(T_2 - T_\infty)}{T_2 - T_\infty}\right)^2 + \left(\frac{U(T_w - T_\infty)}{T_w - T_\infty}\right)^2 + \left(\frac{U(t)}{t}\right)^2 + \left(\frac{U(\lambda)}{\lambda}\right)^2 + \left(\frac{U(c)}{c}\right)^2 \quad (29)$$

The thermocouple has been used for the plenum and mainstream temperature thus the device accuracy has been included to determine the uncertainty for $T_2 - T_\infty$ and $T_w - T_\infty$. At different elapsed time, t both uncertainties for h and η are highly influenced by the $T_2 - T_\infty$ and $T_w - T_\infty$ which mean a different uncertainty should be determined at different η. As the same procedures applied in aerodynamics uncertainties, the uncertainty for η=0.2 and η=0.5 are

$$\left(\frac{U(h)}{h}\right)_{\eta=0.2} = \pm 18.73\% \quad (30)$$

$$\left(\frac{U(\eta)}{\eta}\right)_{\eta=0.2} = \pm 25.49\% \quad (31)$$

$$\left(\frac{U(\eta)}{\eta}\right)_{\eta=0.5} = \pm 15.49\% \quad (32)$$

2.8 Computational fluid dynamics investigation

2.8.1 Upstream leakage flow modeling

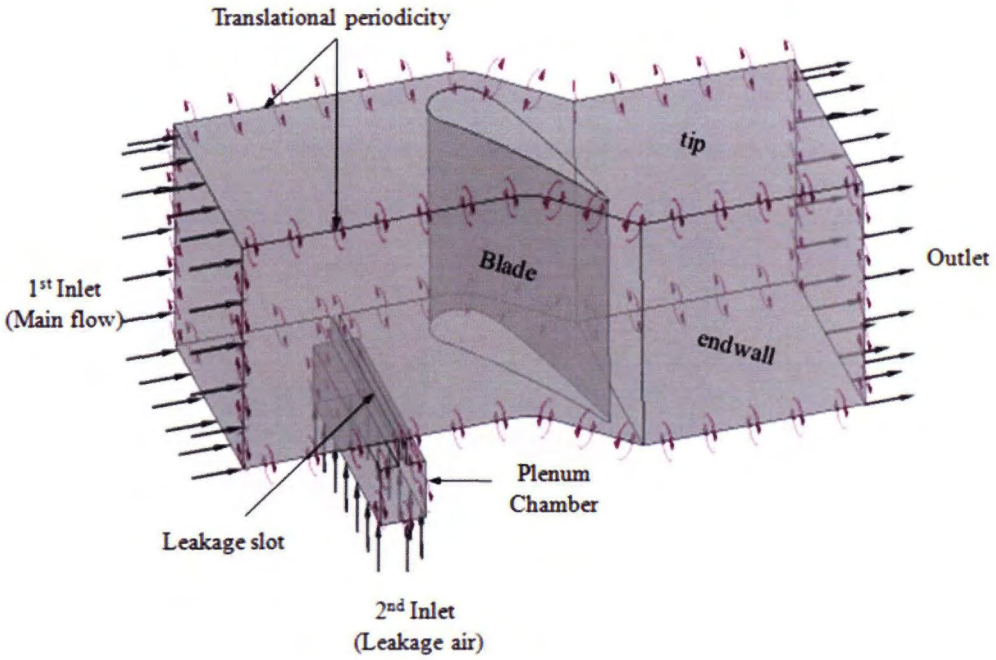

Figure 35 Computational Domain Details

As illustrates in Figure 35, the computational domain for the study of the three dimensional upstream leakage flows in linear cascade flow consisted of the plenum chamber, one pitch endwall domain with a single blade periodicity channel designed by slot located upstream the vane. The computational mesh system was created using Gridgen (Pointwise) to generate a fully structured meshes, see Figure 36. This is a multi-blocks meshing method which consisted of 14 fully structured blocks. The density of mesh cells is increased in the vicinity of the bottom, the top and the blade surfaces but also at injection location. The height of wall-adjacent cells in these regions is 0.02 mm with the objective to obtain y^+ value close to 1 along the walls. The entire computational domain comprises a total of 7.1 million of hexahedral cells. To evaluate the grid independence of the solution, meshes have been tested with a coarser, 5.3 million, and finest of 14.5 million of elements. Domain extended from $2.0C_{ax}$ upstream of the leading edge to $2.0C_{ax}$ downstream of the trailing edge.

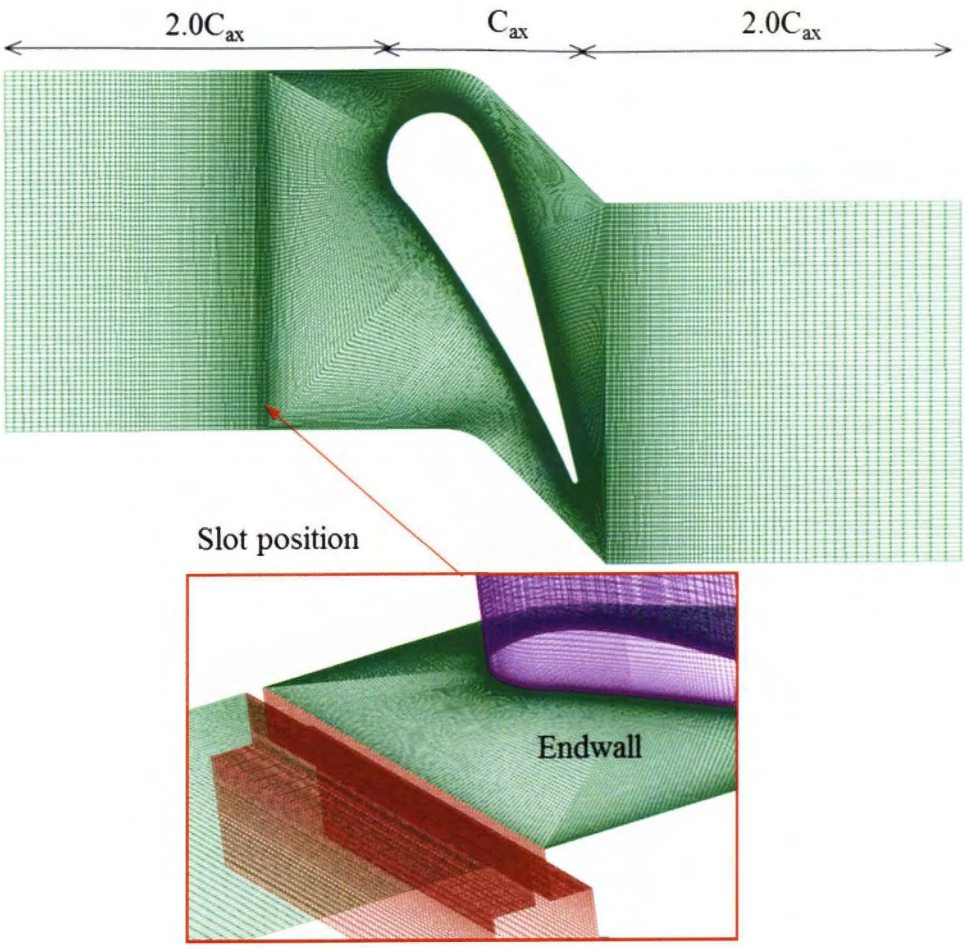

Figure 36 Mesh structures by Gridgen

The boundary conditions are defined in accordance with the measurement conditions for each case. Translational periodic boundary condition was applied on the pitchwise direction. Uniform distributions of measured total pressure and static temperature were specified on the main inlet boundary. As for the leakage flow, the measured mass flow rate and static temperature were specified on the entry plane of the plenum chamber. All walls were treated as adiabatic, no slips walls. However, fixed temperature wall condition was applied for the heat transfer prediction purpose. The simulations were carried out by ANSYS CFX ver. 14 involving Reynolds Average Navier Stokes (RANS) analyses with the employment of shear stress transport (SST) turbulent model. Solution were considered converge when root mean square (RMS) residuals of each transport quantity (mass, momentum, turbulent kinetic

energy and heat transfer) had decreased by at least four order of magnitude and remained approximately constants for at least 1000 iterations.

2.8.2 Grid dependency test

For CFD, by considering the cost and CPU time required, other factors which contribute to the uncertainties in the simulation has been neglected except for the grid number. Figure 37 indicates the spanwise direction of total pressure near the blade downstream to explain the grid number used (7.1 million elements) was quite enough for the flow prediction. The change of the total pressure almost cannot be seen compared to the finest grid with 14.5 million elements. The calculated relative error of the predicted total pressure loss coefficient based on grid number of 7.1 million and 14.5 million elements is approximately 1.6%.

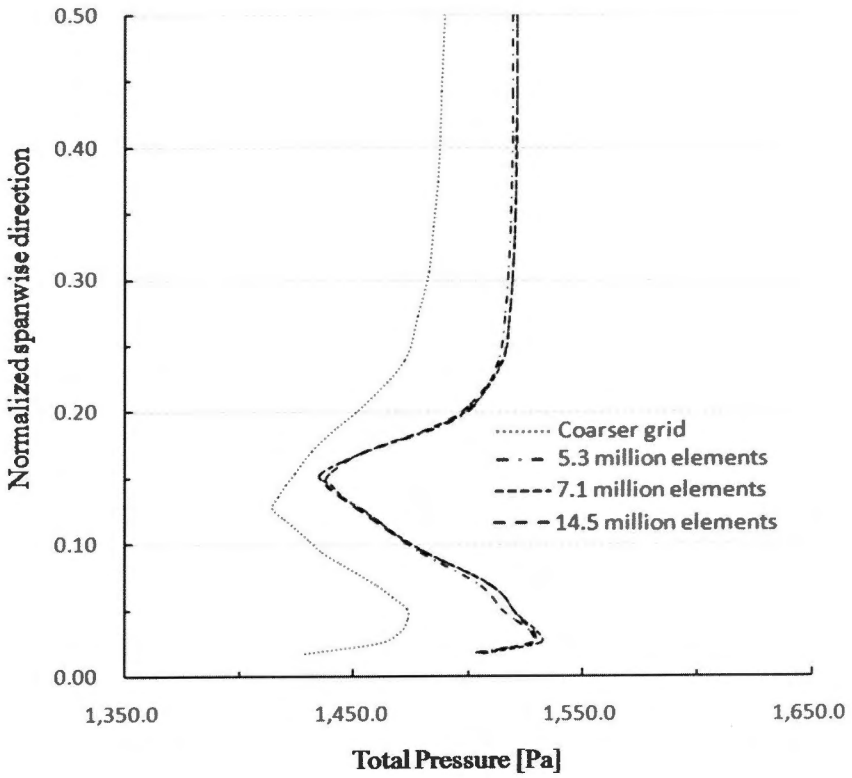

Figure 37 Grid dependency test